Learning to correct climate projection biases

Baoxiang Pan[1], Gemma J. Anderson[1], André Goncalves[1], Donald D. Lucas[1], Céline J.W. Bonfils[1], Jiwoo Lee[1], Yang Tian[1], Hsi-Yen Ma[1]

[1]Lawrence Livermore National Laboratory, Livermore, CA 94550

Key Points:

- Identify and correct climate projection biases using unpaired climate simulation and observation data
- Regularize the data-driven bias corrector using statistical and dynamical constraints
- Significant improvement of daily precipitation estimation regarding a broad range of spatiotemporal statistics

Corresponding author: Baoxiang Pan, pan11@llnl.gov

Abstract

The fidelity of climate projections is often undermined by biases in climate models due to their simplification or misrepresentation of unresolved climate processes. While various bias correction methods have been developed to post-process model outputs to match observations, existing approaches usually focus on limited, low-order statistics, or break either the spatiotemporal consistency of the target variable, or its dependency upon model resolved dynamics. We develop a Regularized Adversarial Domain Adaptation (RADA) methodology to overcome these deficiencies, and enhance efficient identification and correction of climate model biases. Instead of pre-assuming the spatiotemporal characteristics of model biases, we apply discriminative neural networks to distinguish historical climate simulation samples and observation samples. The evidences based on which the discriminative neural networks make distinctions are applied to train the domain adaptation neural networks to bias correct climate simulations. We regularize the domain adaptation neural networks using cycle-consistent statistical and dynamical constraints. An application to daily precipitation projection over the contiguous United States shows that our methodology can correct all the considered moments of daily precipitation at approximately 1° resolution, ensures spatiotemporal consistency and inter-field correlations, and can discriminate between different dynamical conditions. Our methodology offers a powerful tool for disentangling model parameterization biases from their interactions with the chaotic evolution of climate dynamics, opening a novel avenue toward big-data enhanced climate predictions.

Plain Language Summary

Accurate climate prediction is crucial for understanding climate change and implementing effective climate adaptation strategies. However, climate models that are used to generate climate predictions have multifaceted biases that often need to be corrected before predictions can be considered usable. We develop a data-driven methodology that detects and corrects climate model biases using a game theory inspired machine learning technique. By applying physical and statistical constraints, our predictions are not only more accurate, but also more trustworthy as judged by our physical understandings.

1 Introduction

1.1 Two approaches toward improving climate projection accuracy

Understanding, predicting, and adapting to climate change is a problem of growing urgency. These endeavors rely upon climate projections computed by global atmosphere-ocean-land coupled general circulation models (GCMs). Unfortunately, the fidelity of climate projections is often undermined by GCMs' biases due to their over-simplification, coarse grid cells resolution, or misrepresentation of the climate processes (Christensen et al., 2008; Flato et al., 2014; Maraun, 2016; Zelinka et al., 2020).

A solid avenue toward identifying and correcting GCM biases is to apply numerical weather prediction (NWP) techniques to isolate the bias and its propagation from interactions between GCM's parameterized physics and resolved dynamics (Phillips et al., 2004; S. Xie et al., 2012; H.-Y. Ma et al., 2014). This process-oriented diagnostic technique mainly targets GCM biases associated with fast physical processes, such as precipitation, cloud, or convection on short time scales. However, if the bias impact requires longer time scales (1-2 weeks) to develop, this methodology alone may not be sufficient to disentangle the model biases and the unneglectable growth of initial state estimation errors (Smith, 2001).

A separate vein of research, which is more accessible for climate simulation end-users, is to downscale and correct GCM output biases at a post-processing step. The idea is to first establish a statistical connection between GCM's historical simulations and climate observations, and then apply this statistical relationship to reduce their mismatch. Despite several severe problems in their assumptions and implementations (Ehret et al., 2012; Maraun, 2013), these bias correction approaches offer an immediate "improvement" to climate simulations, and have been applied routinely in a broad range of applications, such as climate change impact analysis (Wood et al., 2004; H. Li et al., 2010), and climate-related decision making (Teutschbein & Seibert, 2012; L. Li et al., 2015).

The key difficulty for bias correction lies in that, due to the chaotic nature of geophysical fluid dynamics, the freely evolving historical climate simulations do not follow the evolution of historical climate variability. This prevents us from inferring GCM biases by contrasting simulation-observation time series, as is conventionally done in weather-to-seasonal forecast verification (F. Ma et al., 2016; Pan, Hsu, AghaKouchak, Sorooshian, & Higgins, 2019; Zhao et al., 2021). Correspondingly, we usually infer biases by comparing simulated and observed climate mean state or other simple statistics summarized over a long range period (i.e., multiple decades). On one hand, this conceals detailed bias information that is canceled out through error compensations. On the other hand, this leaves us with limited observational climatology references to develop and verify powerful bias identification and correction algorithms. Consequently, existing bias correction practices tend to conceal, rather than correct the GCM biases.

1.2 What counts as a "perfect" climate projection bias corrector?

In a critical discussion of bias correction applicability, Ehret et al. (2012) requires a "perfect" bias correction approach to be able to:

1. *correct at high spatiotemporal resolution all moments of the variable of interest,*
2. *assure spatiotemporal consistency as well as inter-field correlations,*
3. *discriminate between different weather situations, allow for the bias to be time-transient,*
4. *include feedback effects.*

To meet these requirements, they conclude that we will *"inevitably arrive at a complexity of the bias correction method comparable to the GCM itself, but still lack the physical justification of the latter"* (Ehret et al., 2012).

While we agree with this conclusion, here we use this statement as guidance to formulate the GCM bias correction task as a machine learning problem. That is, to identify and correct GCM biases, we need powerful black-box models that can tackle problems whose complexity is comparable to that of GCMs, and come up suitable objective functions to train these black-box models toward the above listed requirements.

The high requirement on the capability of black-box models is no longer an obstacle. Recent years have witnessed the flourishing of deep learning that successfully solves complex, high-dimensional problems, including physical system simulations such as electromagnetic and fluid dynamics (Mills et al., 2017; Kutz, 2017), as well as climate applications such as parameterization (Rasp et al., 2018; Pan, 2019), downscaling (Pan, Hsu, AghaKouchak, & Sorooshian, 2019; Miao et al., 2019), analog forecasting (Weyn et al., 2019; Pan, Anderson, Goncalves, et al., 2020), inverse modeling (Zhang et al., 2020), and climate signal identification (Barnes et al., 2019).

While most of the applications above adopt a supervised learning problem setting, which maps an input to an output by learning from example input-output pairs, we do not have paired GCM simulations and observations to learn GCM biases, except in very

limited retrospective forecast cases (Phillips et al., 2004; Rasp & Lerch, 2018). On one hand, it is difficult, if not impossible, to train powerful data-driven models with these limited paired data. On the other hand, we can not afford hindcast based diagnosis for each GCM configuration. Is it possible to learn GCM biases from large amount unpaired historical climate simulation and observation data?

1.3 Correct climate projection biases using *adversarial learning*

We demonstrate that *adversarial learning* (Goodfellow et al., 2014) is a less-exploited, yet well-suited paradigm for identifying and correcting climate projection biases using unpaired simulation and observation data. Rather than pre-assuming the spatiotemporal characteristics of the model biases, we carefully design a discriminative function to identify arbitrary mismatches between the distribution of climate simulations and observations. Feedback from this discriminative function is applied to learn a bias correction function to close these mismatches. We alternatively train the discriminative function and the bias correction function to improve the skills of both, until the corrected climate simulation is indistinguishable from the observation. This *adversarial learning* framework offers the potential for leveraging the big data of historical climate observations and simulations to disentangle the parameterization biases with model resolved dynamics, saving the huge effort in forcing a GCM to start from realistic initial conditions to expose its parameterization biases.

Although promising, *adversarial learning* can be highly unconstrained (Yang et al., 2019; Wu et al., 2020; Pan, Anderson, Lucas, et al., 2020). For instance, the bias correction function may map the GCM simulations to limited varieties of climate variability modes, or result in "corrections" that are inconsistent with GCM resolved dynamics. To address these issues, we introduce several statistical and dynamical constraints to regularize the data-driven bias corrector. We show that the Requirements 1-3 in Ehret et al. (2012) can potentially be well satisfied using this regularized adversarial domain adaptation (RADA) methodology. To include feedback effects (Requirement 4), we should either couple the bias corrector with dynamical simulations, or iteratively apply this methodology to correct the parameterization biases and alleviate their impacts on model resolved dynamics. We discuss the difficulties and opportunities here, and leave the tackling of the feedback problem (Requirement 4) for future work.

The rest of the paper is organized as follows. First, in Section 2, we introduce the notion of *adversarial learning*, the challenges of using an unregularized methodology, as well as the three regularization methods. A case study for correcting daily precipitation projection bias is presented in Section 3, and the results of this case study are described in Section 4. Section 5 discusses the individual and combined contributions of the three regularizers to improve the *adversarial learning* of GCM biases. Section 6 compares our approach with well-established univariate and multivariate bias correction methods. Section 7 discusses the perceptual performance and the training stopping criteria of the RADA methodology. We draw conclusions and layout the direction for future work in Section 8.

2 Methodology

2.1 Disentangle parameterization and dynamics using GAN

We distinguish two sets of variables in climate simulation. The first set includes the variables that are directly resolved by discretizing the geophysical fluid dynamical equations, also informally referred to as the *dynamics*. The second set includes the remaining unresolved variables, also informally referred to as the *physics*. In climate simulation, the unresolved variables are estimated based on their statistical connections with the resolved variables. These parameterization processes contribute to the majority of

climate simulation biases. Our objective is to identify and correct these parameterization biases. The challenge lies in disentangling the intricate parameterization biases from their interactions with the chaotic evolution of climate dynamics.

To efficiently address this challenge, we introduce the generative adversarial neural network (GAN, Goodfellow et al. 2014), which serves as the backbone of our data-driven bias correction methodology. In GANs, a neural network parameterized function, named the generator (G, see supporting information for notation clarification), learns a mapping from random noise to a target distribution, while an auxiliary neural network parameterized function, named the discriminator (D), guides the training of G by distinguishing candidates produced by G from the target distribution. The term *adversarial learning* refers to the idea that, G is not trained toward a pre-defined, fixed objective, but to fool D, which itself is dynamically updated to enhance its discrimination capability.

Here, instead of applying GANs to generate new samples, we make use of the *adversarial learning* idea to match samples from a source domain to corresponding samples in a target domain. This line of research is often named *domain adaptation* or *domain translation* in the machine learning literature (Zhu et al., 2017; Liu et al., 2017; Tzeng et al., 2017; Wang et al., 2018; Wilson & Cook, 2020). Specifically, as is illustrated in Fig. 1, we apply G as a deterministic bias correction function that translates samples from a source domain $\mathbf{X}$ to their corresponding analog samples in a target domain $\mathbf{Y}$, where $\mathbf{X}$ is GCM simulation of a target, parameterized variable (i.e., precipitation, Fig. 1 bottom left), $\mathbf{Y}$ is its observation (Fig. 1 top left). We train D to distinguish whether a sample comes from $\mathbf{Y}$ or $G(\mathbf{X})$ by minimizing a discrimination error (Fig. 1 blue arrow, strict formulation provided latter). The evidences based on which D makes distinctions are applied to train G to make $G(\mathbf{X})$ less distinguishable from $\mathbf{Y}$ (Fig. 1 red arrow, strict formulation provided latter), hence closing the mismatch between the distributions of $\mathbf{X}$ and $\mathbf{Y}$.

How can we guarantee D distinguishes $\mathbf{Y}$ and $G(\mathbf{X})$ relying purely upon the GCM parameterization bias information, not the uncontrollable dynamical state variance information? We explain two critical configurations that make D work here. First, we suppress the irrelevant dynamical variance signal: we train D using $\mathbf{Y}$ and $G(\mathbf{X})$ samples with random dynamical states (Fig. 1 wave arrows). Since the dynamical state differences do not contribute to the discrimination objective, D will learn representations that suppress the impact of samples' dynamical state variances, and turn to the parameterization bias information to distinguish $\mathbf{Y}$ and $G(\mathbf{X})$. Second, we enhance the parameterization bias signal: we consider large spatial patterns (i.e., continental scale in Fig. 1) of the target variable, rather than pixel-by-pixel values, to distinguish the parameterization bias signal. This is inspired by Barnes et al. (2019) and Sippel et al. (2020), which tell that, intricate climate signals, when viewed from large spatial scale, are more detectable.

In practice, we use the Wasserstein GAN (Arjovsky et al. 2017, see supporting information for details), given its training stability. Specifically, we consider D with continuous output expressing how likely a sample is from $\mathbf{Y}$ rather than $G(\mathbf{X})$. We alternatively train G to increase the false positive rate of $G(\mathbf{X})$ being taken as $\mathbf{Y}$, and train D to enhance the distinction between $G(\mathbf{X})$ and $\mathbf{Y}$. These are achieved by applying stochastic gradient descent/ascent toward the following min/max objective:

$$\min_{G} \max_{D} \mathbb{E}_{\mathbf{y}\sim p_{\mathbf{Y}}}\big[D(\mathbf{y})\big] - \mathbb{E}_{\mathbf{x}\sim p_{\mathbf{X}}}\big[D\big(G(\mathbf{x})\big)\big] \tag{1}$$

Here $\mathbb{E}_{\mathbf{y}\sim p_{\mathbf{Y}}}$ and $\mathbb{E}_{\mathbf{x}\sim p_{\mathbf{X}}}$ are expectations taken over probability distribution of $\mathbf{Y}$ and $\mathbf{X}$. Competition between G and D driven by stochastic gradient descent/ascent improves the skills of both, until the distribution of $G(\mathbf{X})$ is indistinguishable from $\mathbf{Y}$ as viewed by D. This *adversarial learning* framework automatically identifies multifaceted mismatches between domain distributions, and simultaneously reduces the distribution mismatches.

2.2 Regularizing the *adversarial learning* process

2.2.1 Necessity for regularization

The adversarial loss in Eq. 1 serves as a general, high-level objective for correcting GCM biases. Various solutions can meet this *adversarial learning* objective. However, many of them may appear authentic upon visual inspection, but are physically unreasonable. Specifically, we may face the following three challenges:

1. **Mode collapse**. G may map the GCM simulations to limited varieties of climate variability, lacking diversity as compared to the uncorrected simulations. An extreme example is that, G maps all simulations to a same, observation-alike output. This situation satisfies the adversarial learning objective in Eq. 1 well, but yields biased, less-diverse distribution estimation.
2. **Dynamical inconsistency**. This means that, even if $G(\mathbf{x})$ is statistically indistinguishable from samples of $\mathbf{Y}$, the resulting $G(\mathbf{x})$ may not be physically consistent with the GCM's resolved dynamics. Enforcing dynamical consistency implicitly alleviates mode collapse.
3. **Dynamical invariance**. For two same GCM simulation samples, if their embedding dynamical conditions are different, they may exhibit distinct mismatches with observations. It is difficult to discriminate dynamics-dependent biases, if the bias corrector is not conditioned on the resolved dynamics.

These three challenges roughly correspond to the Requirement 1-3 in Ehret et al. (2012). To overcome these challenges, we introduce three corresponding statistical and dynamical regularizers to constrain G in *adversarial learning* for correcting GCM biases. Here regularization refers to adding extra information to exclude physically unreasonable solutions in an ill-posed optimization problem. Part of the introduced regularizers here are well-established tools developed by the machine learning community (Sec. 2.2.2), while the rest are uniquely designed for the climate projection bias correction problem (Sec. 2.2.3 and 2.2.4). We demonstrate the benefits of these regularizers with ablation analysis in the latter introduced case study (Sec. 5).

2.2.2 Cycle consistency

We alleviate the mode collapse problem using the cycle consistency regularization, which has quickly become the de facto regularization method for learning GAN-based domain adaptation (Zhu et al., 2017; Kim et al., 2017). The idea is to enforce one-to-one correspondence between domains by coupling an adversarial domain adaptation model $\{G, D\}$ with its inverse model $\{G^{-1}, D^{-1}\}$. In this inverse model, G^{-1} maps $\mathbf{Y}$ back to $\mathbf{X}$, and D^{-1} guides the learning of G^{-1} by distinguishing samples from $\mathbf{X}$ and $G^{-1}(\mathbf{Y})$. To couple the two opposite-directed adversarial learning processes, we minimize the following cycle consistency loss $\mathcal{L}_C$ besides the adversarial losses (Zhu et al., 2017):

$$\mathcal{L}_C = \mathbb{E}_{\mathbf{x}\sim p_{\mathbf{X}}}\Big(||G^{-1}\big(G(\mathbf{x})\big) - \mathbf{x}||_1\Big) + \mathbb{E}_{\mathbf{y}\sim p_{\mathbf{Y}}}\Big(||G\big(G^{-1}(\mathbf{y})\big) - \mathbf{y}||_1\Big) \tag{2}$$

Here, $||\cdot||_1$ is the L^1-norm, which has shown to work better than L^2-norm, as it tends to produce sharper results (Zhu et al., 2017). To minimize $\mathcal{L}_C$ pushes $G^{-1}\big(G(\mathbf{X})\big) \approx \mathbf{X}$ and $G\big(G^{-1}(\mathbf{Y})\big) \approx \mathbf{Y}$, which encourages learning invertible mappings between $\mathbf{X}$ and $\mathbf{Y}$.

The physical explanation for enforcing invertible mapping is that, provided with a same resolvable, underlying dynamical state $\mathbf{s}$, the GCM simulation of a target variable is preferred to be identical to its observation (we neglect stochastic parameterization noise here, and revisit this issue in Sec. 8.2.1.) Given a same set of plausible dynamical states $\mathbf{S}$ subjected to certain external forcing, an optimal domain adaptation func-

tion G should be invertible as bridged by $\mathbf{S}$. Therefore, if the GCM historical simulation can generate a same range of climate dynamical state as the observed climate system, we can translate $\mathbf{X}$ to $G(\mathbf{X})$ that is distributed nearly identically to $\mathbf{Y}$.

Since this neural network based methodology can easily scale up to high dimensional massive data (Bottou, 2010), by matching the distribution of $G(\mathbf{X})$ and $\mathbf{Y}$, we can automatically correct at high spatiotemporal resolution all moments of the variable of interest (Requirement 1 in Ehret et al. 2012).

2.2.3 Dynamical consistency

Although cycle consistency helps to restrict the learning to a smaller feasible solution space of invertible functions, we may still end up finding many invertible mappings between the two considered domains (see Cohen et al. 2018 for a failure case example). To guarantee that an individual climate simulation sample $\mathbf{x}$ is meaningfully translated to its corresponding analog sample in $\mathbf{Y}$, we should have $\mathbf{x}$ and $G(\mathbf{x})$ correspond to a same dynamical state $\mathbf{s_x}$. We enforce this by maintaining the inter-field consistency between the target variable and its underlying dynamical state during training.

To achieve dynamical consistency, we first build statistical models that estimate the target variable ($\mathbf{X}$ and $\mathbf{Y}$) using its underlying dynamical state information ($\mathbf{S_X}$ and $\mathbf{S_Y}$, see supporting information for details):

$$\begin{aligned} F^*_{\mathbf{X}} &= \underset{F_{\mathbf{X}}}{\operatorname{argmin}}\ \mathbb{E}_{\mathbf{x}\sim p_{\mathbf{X}}}\big(||F_{\mathbf{X}}(\mathbf{s_x}) - \mathbf{x}||_2\big) \\ F^*_{\mathbf{Y}} &= \underset{F_{\mathbf{Y}}}{\operatorname{argmin}}\ \mathbb{E}_{\mathbf{y}\sim p_{\mathbf{Y}}}\big(||F_{\mathbf{Y}}(\mathbf{s_y}) - \mathbf{y}||_2\big) \end{aligned} \tag{3}$$

Here $F^*_{\mathbf{X}}$ and $F^*_{\mathbf{Y}}$ are arbitrary form (i.e., neural network, see supporting information) statistical models developed for the GCM simulated climate system and the observed climate system; $\mathbf{s_x}$ and $\mathbf{s_y}$ are dynamical state representations corresponding to $\mathbf{x}$ and $\mathbf{y}$, which are typically resolvable variables not directly impaired by GCM biases. $F^*_{\mathbf{X}}$ and $F^*_{\mathbf{Y}}$ are often known as statistical downscaling models, as they derive statistical relationships between small-scale, parameterized variables and large-scale, resolved dynamics. The purpose for developing and applying these models here is not to enhance resolution, but to ensure the consistency between $G(\mathbf{X})$ and $\mathbf{S_X}$, $G^{-1}(\mathbf{Y})$ and $\mathbf{S_Y}$, which is described below.

We use the resulting $F^*_{\mathbf{X}}$ and $F^*_{\mathbf{Y}}$ to constrain G and G^{-1} by minimizing the following dynamical consistency loss $\mathcal{L}_D$:

$$\mathcal{L}_D = \mathbb{E}_{\mathbf{x}\sim p_{\mathbf{X}}}\big[\max\big(||F^*_{\mathbf{Y}}(\mathbf{s_x}) - G(\mathbf{x})||_2, \delta_{\mathbf{Y}}\big) - \delta_{\mathbf{Y}}\big] + \mathbb{E}_{\mathbf{y}\sim p_{\mathbf{Y}}}\big[\max\big(||F^*_{\mathbf{X}}(\mathbf{s_y}) - G^{-1}(\mathbf{y})||_2, \delta_{\mathbf{X}}\big) - \delta_{\mathbf{X}}\big] \tag{4}$$

Here $\delta_{\mathbf{X}} = \mathbb{E}_{\mathbf{x}\sim p_{\mathbf{X}}}\big(||F^*_{\mathbf{X}}(\mathbf{s_x}) - \mathbf{x}||_2\big)$, $\delta_{\mathbf{Y}} = \mathbb{E}_{\mathbf{y}\sim p_{\mathbf{Y}}}\big(||F^*_{\mathbf{Y}}(\mathbf{s_y}) - \mathbf{y}||_2\big)$, which are the L^2 regression losses of the statistical models $F^*_{\mathbf{X}}$ and $F^*_{\mathbf{Y}}$. By minimizing $\mathcal{L}_D$, we impose the inter-field correlation of $\{\mathbf{X}, \mathbf{S_X}\}$ and $\{\mathbf{Y}, \mathbf{S_Y}\}$ to $\{G^{-1}(\mathbf{Y}), \mathbf{S_Y}\}$ and $\{G(\mathbf{X}), \mathbf{S_X}\}$, penalizing errors beyond the statistical downscaling constraints quantified by $\delta_{\mathbf{X}}$ and $\delta_{\mathbf{Y}}$. Here, we tolerate errors smaller than $\delta_{\mathbf{X}}$ and $\delta_{\mathbf{Y}}$: if $||F^*_{\mathbf{Y}}(\mathbf{s_x}) - G(\mathbf{x})||_2$ and $||F^*_{\mathbf{X}}(\mathbf{s_y}) - G^{-1}(\mathbf{y})||_2$ are smaller than $\delta_{\mathbf{Y}}$ and $\delta_{\mathbf{X}}$, $\mathcal{L}_D$ diminishes to 0. This setting admits the fact that $\mathbf{X}$ and $\mathbf{Y}$ are not uniquely determined by $\mathbf{S_X}$ and $\mathbf{S_Y}$, and avoids the bias corrector from producing the mean of all possible outcomes, leaving space for optimizing the adversarial loss (Eq. 1) within the dynamical consistency constraint.

To minimize $\mathcal{L}_D$ loosely guarantees that $G(\mathbf{X})$ and $G^{-1}(\mathbf{Y})$ are consistent with their underlying dynamical states $\mathbf{S_X}$ and $\mathbf{S_Y}$. Also, this constraint implicitly encourages spatiotemporal consistency of the target variable, and further alleviates mode collapse. Provided that $F^*_{\mathbf{X}}$ and $F^*_{\mathbf{Y}}$ can impose strong constraints on the variability of $\mathbf{X}$ and $\mathbf{Y}$, which

has been intensively testified by statistical downscaling studies (Pan, Hsu, AghaKouchak, & Sorooshian, 2019; Miao et al., 2019; Sun & Tang, 2020), we could guarantee the inter-field correlation as well as the spatiotemporal consistency of the bias correction. The Requirement 2 in Ehret et al. (2012) can thus be fulfilled.

2.2.4 Dynamical dependency

Biases in GCM simulations in part depend on the underlying dynamics. For instance, consider a common GCM bias of overestimating the number of wet days (Piani et al., 2010), the knowledge of the dynamical state helps identifying if a simulated drizzle event is a case of false alarm or true positive. This suggests that the bias correction function G should take into consideration of both the target variable $\mathbf{X}$ and the dynamical state $\mathbf{S_X}$. Similarly, G^{-1} should take into input of both $\mathbf{Y}$ and $\mathbf{S_Y}$. As we make G and G^{-1} functions of $(\mathbf{S_X}, \mathbf{X})$ and $(\mathbf{S_Y}, \mathbf{Y})$, we can potentially discriminate between different weather situations, allowing the bias corrector to be time-transient (Requirement 3 in Ehret et al. 2012).

2.3 Regularized Adversarial Domain Adaptation

We summarize the final bias correction methodology here: as is illustrated in Fig. 2a, we apply two discriminative neural networks D and D^{-1} to learn arbitrary mismatch between the distribution of historical climate simulation $\mathbf{X}$ and observation $\mathbf{Y}$. Meanwhile, we adopt dynamics-dependent domain adaptation neural networks $G(\mathbf{X}, \mathbf{S_X})$ and $G^{-1}(\mathbf{Y}, \mathbf{S_Y})$ to close the mismatch under cycle consistency constraint and dynamical consistency constraint. The final objective function of this regularized adversarial domain adaptation (RADA) bias corrector takes the following form:

$$
\begin{aligned}
\mathcal{L}_{\mathrm{RADA}} = & \underbrace{\mathbb{E}_{\mathbf{y}\sim p_{\mathbf{Y}}}\left[D(\mathbf{y})\right] - \mathbb{E}_{\mathbf{x}\sim p_{\mathbf{X}}}\left[D\big(G(\mathbf{x}, \mathbf{s_x})\big)\right]}_{\text{(i) Adversarial loss for } \mathbf{X}\to\mathbf{Y}} + \underbrace{\mathbb{E}_{\mathbf{x}\sim p_{\mathbf{X}}}\left[D^{-1}(\mathbf{x})\right] - \mathbb{E}_{\mathbf{y}\sim p_{\mathbf{Y}}}\left[D^{-1}\big(G^{-1}(\mathbf{y}, \mathbf{s_y})\big)\right]}_{\text{(ii) Adversarial loss for } \mathbf{Y}\to\mathbf{X}} \\
& + \lambda_C \underbrace{\left[\mathbb{E}_{\mathbf{x}\sim p_{\mathbf{X}}}\Big(||G^{-1}\big(G(\mathbf{x}, \mathbf{s_x}), \mathbf{s_x}\big) - \mathbf{x}||_1\Big) + \mathbb{E}_{\mathbf{y}\sim p_{\mathbf{Y}}}\Big(||G\big(G^{-1}(\mathbf{y}, \mathbf{s_y}), \mathbf{s_y}\big) - \mathbf{y}||_1\Big)\right]}_{\text{(iii) } \mathcal{L}_C\text{: Cycle consistency loss}} \\
& + \lambda_D \underbrace{\left[\mathbb{E}_{\mathbf{x}\sim p_{\mathbf{X}}}\left[\max\big(||F^*_{\mathbf{Y}}(\mathbf{s_x}) - G(\mathbf{x}, \mathbf{s_x})||_2, \delta_{\mathbf{Y}}\big) - \delta_{\mathbf{Y}}\right] + \mathbb{E}_{\mathbf{y}\sim p_{\mathbf{Y}}}\left[\max\big(||F^*_{\mathbf{X}}(\mathbf{s_y}) - G^{-1}(\mathbf{y}, \mathbf{s_y})||_2, \delta_{\mathbf{X}}\big) - \delta_{\mathbf{X}}\right]\right]}_{\text{(iv) } \mathcal{L}_D\text{: Dynamical consistency loss}}
\end{aligned}
\tag{5}
$$

$\mathcal{L}_{\mathrm{RADA}}$ includes the following four components: (i) the adversarial loss for mapping $\mathbf{X}$ to $\mathbf{Y}$, (ii) the adversarial loss for the inverse mapping from $\mathbf{Y}$ to $\mathbf{X}$, (iii) the cycle consistency loss, and (iv) the dynamical consistency loss. We weigh these losses using hyperparameters λ_C and λ_D.

To train the RADA model, we first train $F_{\mathbf{X}}$ and $F_{\mathbf{Y}}$ to minimize the statistical downscaling loss, then, we fix the trained models $F^*_{\mathbf{X}}$ and $F^*_{\mathbf{Y}}$, and alternatively train $\{G, G^{-1}\}$ to minimize (i)-(iv), and train $\{D, D^{-1}\}$ to maximize (i) and (ii). Unlike supervised learning, where we stop training as the supervision loss reaches a minimum for the validation set, there is no consensus about when the adversarial training obtains optimal performance, and the training should be terminated. A common strategy is to visually inspect the generated results and stop the training if there is no visually perceived improvement. However, as we will show in Sec. 7, this strategy does not work in our problem, as perceptual judgements can be easily fooled, and yield poor quantitative performance during test. Here, we compare some crucial precipitation indices (first to fourth order moments, see Sec. 3.4 for details) between corrected simulations and observations for the validation set at the end of each training epoch, and terminate the training when these statistics match best.

3 Experimental design

3.1 General settings

To test the proposed methodology, we consider a case study of correcting the Community Earth System Model version 2 (CESM2, Danabasoglu et al. 2020) daily precipitation projection over the contiguous United States (CONUS). We consider precipitation because it is among the most important yet least well-simulated variables in GCMs (Marvel & Bonfils, 2013; Tapiador et al., 2019). Later studies may explore the possibility of scaling up this methodology from univariate fields to multivariate fields, from continental scale to global scale, and from moderate spatiotemporal resolution to high resolution, by leveraging the scalability of deep neural networks.

We quantify the precipitation estimation accuracy before and after correction using a suite of commonly applied skill indices computed for a holdout test set. The applied data, data processing methods, model configuration, and evaluation approaches are described below.

3.2 Data

3.2.1 GCM simulation

CESM2 is an open-source, fully-coupled, global climate model that provides state-of-the-art computer simulations of the Earth's past, present, and future climate states (Danabasoglu et al., 2020). We use CESM2 historical simulation contributing to the Coupled Model Intercomparison Project phase 6 (CMIP6, Eyring et al. 2016). Besides the daily precipitation products, we use the simulated daily averaged sea level pressure (SLP), geopotential height and specific humidity at 500 hPa ($z_{500\text{hPa}}$ and $q_{500\text{hPa}}$) as dynamical constraints to support model training (Pan, Hsu, AghaKouchak, & Sorooshian, 2019). All the simulation data are of a common resolution of approximately 1°.

3.2.2 Observation

We use the U.S. National Oceanic and Atmospheric Administration (NOAA) Climate Prediction Center (CPC) unified gauge-based analysis of daily precipitation over CONUS (0.25°, P. Xie et al. 2010) as observational reference for bias correction. The daily averaged SLP, $z_{500\text{hPa}}$ and $q_{500\text{hPa}}$ records from the European Centre for Medium-Range Weather Forecasts (ECMWF) atmospheric reanalysis of the 20th century (ERA-20C, 1.25°, Poli et al. 2016) are used as dynamical constraints for the observations.

3.2.3 Data processing

The precipitation field data covering CONUS (25°N-50°N, 65°W-125°W) land areas are used. We apply the dynamical field data with an extra 5° spatial extension (20°N-55°N, 60°W-130°W) to constrain the precipitation field. The observed precipitation, SLP, $z_{500\text{hPa}}$ and $q_{500\text{hPa}}$ reanalyses are regridded to the same resolution as CESM2 simulation using bi-linear spatial averaging (for CPC precipitation observation) or interpolation (for ERA-20C). To accommodate the long-tail distribution nature of precipitation, we regularize the precipitation data using a natural logarithm transformation. We normalize the dynamical variables by subtracting the grid mean, and dividing by the grid standard deviation. It should be noted that, different data processing approaches might influence the model performance. We leave a detailed examination on the impact of data processing for future work.

We split the data into training, validation, and test sets. The training and validation sets cover the period of 1950 to 1994 (16,435 days). To sample different climate periods for model training, for each decade from 1950 to 1994, we put data from the first

8 years into the training set, and the remaining 2 years into the validation set. Data from 1995 to 2004 (3,652 days) are held out in the test set to offer unbiased evaluation of the bias corrector.

3.3 Model configuration

The RADA model architecture is illustrated in Fig. 2. We apply convolutional neural networks (CNNs, LeCun et al. 1995; Krizhevsky et al. 2012) as building blocks for the model, given their capability to exploit the multi-scale spatial coherency of geodata (Pan, Hsu, AghaKouchak, & Sorooshian, 2019; Baño-Medina et al., 2020; Sadeghi et al., 2020).

For the downscaling submodules of $F^*_{\mathbf{X}}$ and $F^*_{\mathbf{Y}}$, we apply a U-net form of CNN (Fig. 2b, Ronneberger et al. 2015). The U-net applies a convolution based contracting path to capture the resolved dynamical field information, and a symmetric transposed convolution based expanding path that gradually refines precipitation field estimation. Skip connections between symmetrical convolution and transposed convolution blocks ease the training by forcing the deeper layers to learn meaningful representations that are not well captured by shallower layers (He et al., 2016). Similarly, we apply CNNs with skip connections for $\{G, G^{-1}\}$ (Fig. 2c) and $\{D, D^{-1}\}$ (Fig. 2d).

We use the Adam optimizer (Kingma & Ba, 2014) with batch size of 32, learning rate of 10^{-4}, and train the model for 300 epochs using 36 GPUs on the *Wolfram Mathematica* 12.1 deep learning platform (Wolfram Research, Inc., n.d.). The training does not require the climate simulation and observation data to be synchronized. Considering the impact of seasonal cycle, internal climate variability, and climate change, in each iteration of a training epoch, we take random mini-batch of daily precipitation observations, and sample climate simulations from the same months and ± 5 years. This strategy greatly increases the training sample diversity, while excludes the impact of seasonality and climate change. For each training epoch, we shuffle the observational data in the training set, split the data into random mini-batches. For each mini-batch, we sample the corresponding simulation data (same months and ± 5 years), obtain the gradient of $\mathcal{L}_{\mathrm{RADA}}$ with respect to all the model parameters using this mini-batch of data, and update the model parameters accordingly. We repeat this process for all the mini-batches, completing one epoch of training.

We take an ensemble of trained neural networks, each representing a condition where no individual index measuring the precipitation estimation accuracy can be improved without worsening other indices (Pareto front). The considered indices are the spatial average root mean square error between observation's and simulation's first to fourth order moment of precipitation distribution (see Sec. 3.4). The average of the four neural network outputs are applied as the final bias correction result.

3.4 Performance evaluation

The discriminator D can in principle detect any mismatch between the distribution of observations and simulations, given that neural networks are universal function approximators (Leshno et al., 1993). Therefore, we could potentially evaluate the bias correction performance based on any statistics. Here we focus on the commonly applied measure of precipitation distribution characteristics, including the moments, quantile, frequency, intensity, and seasonality characteristics at grid scale, as well as spatial coherency and dynamical consistency at field scale. The considered indices are listed in Tab. 1.

For grid scale assessment, we consider the first to fourth order moments (mean, standard deviation, skewness, and kurtosis), the three tertiles (33%, 66%, 99% quantile), the probability of precipitation, the average precipitation intensity, the 1-day, 3-day, and 5-day maximum precipitation, ratio of winter/summer (December-February/June-August)

Table 1. Indices for assessing the bias correction performance

Scale	Scope	Statistics	Calculation
Grid	Moment	Mean (μ)	$\mathbb{E}_{\mathbf{y}\sim p_{\mathbf{Y}}}(\mathbf{y})$, $\mathbb{E}_{\mathbf{x}\sim p_{\mathbf{X}}}(\mathbf{x})$, $\mathbb{E}_{\mathbf{x}\sim p_{\mathbf{X}}}(G(\mathbf{x}))$
		Standard deviation (σ)	$\sqrt{\mathbb{E}_{\mathbf{y}\sim p_{\mathbf{Y}}}(\mathbf{y}-\mu_{\mathbf{Y}})^2}$, $\sqrt{\mathbb{E}_{\mathbf{x}\sim p_{\mathbf{X}}}(\mathbf{x}-\mu_{\mathbf{X}})^2}$, $\sqrt{\mathbb{E}_{\mathbf{x}\sim p_{\mathbf{X}}}(G(\mathbf{x})-\mu_{G(\mathbf{X})})^2}$
		Skewness (Skew)	$\mathbb{E}_{\mathbf{y}\sim p_{\mathbf{Y}}}(\frac{\mathbf{y}-\mu_{\mathbf{Y}}}{\sigma_{\mathbf{Y}}})^3$, $\mathbb{E}_{\mathbf{x}\sim p_{\mathbf{X}}}(\frac{\mathbf{x}-\mu_{\mathbf{X}}}{\sigma_{\mathbf{X}}})^3$, $\mathbb{E}_{\mathbf{x}\sim p_{\mathbf{X}}}(\frac{G(\mathbf{x})-\mu_{G(\mathbf{X})}}{\sigma_{G(\mathbf{X})}})^3$
		Kurtosis (Kurt)	$\mathbb{E}_{\mathbf{y}\sim p_{\mathbf{Y}}}(\frac{\mathbf{y}-\mu_{\mathbf{Y}}}{\sigma_{\mathbf{Y}}})^4$, $\mathbb{E}_{\mathbf{x}\sim p_{\mathbf{X}}}(\frac{\mathbf{x}-\mu_{\mathbf{X}}}{\sigma_{\mathbf{X}}})^4$, $\mathbb{E}_{\mathbf{x}\sim p_{\mathbf{X}}}(\frac{G(\mathbf{x})-\mu_{G(\mathbf{X})}}{\sigma_{G(\mathbf{X})}})^4$
	Quantile	1-3 tertile ($Q_{33\%,66\%,99\%}$)	33%, 66%, 99% quantile
	Frequency	Probability of precipitation (PoP)	$\frac{\text{Total precipitation days}}{\text{Total days}}$
	Intensity	Average intensity (Int)	$\mathbb{E}_{\mathbf{Y}>0}(\mathbf{y})$, $\mathbb{E}_{\mathbf{X}>0}(\mathbf{x})$, $\mathbb{E}_{G(\mathbf{X})>0}\big(G(\mathbf{x})\big)$
		1-day max ($\max_1$)	$\max(\mathbf{y})$, $\max(\mathbf{x})$, $\max\big(G(\mathbf{x})\big)$
		3-day max ($\max_3$)	$\max(\sum_i^{i+2}\mathbf{y}_i)$, $\max(\sum_i^{i+2}\mathbf{x}_i)$, $\max\big(\sum_i^{i+2}G(\mathbf{x}_i)\big)$
		5-day max ($\max_5$)	$\max(\sum_i^{i+4}\mathbf{y}_i)$, $\max(\sum_i^{i+4}\mathbf{x}_i)$, $\max\big(\sum_i^{i+4}G(\mathbf{x}_i)\big)$
	Seasonality	Winter precipitation ratio (R_{W})	$\frac{\text{Dec-Feb precipitation}}{\text{Total precipitation}}$
		Summer precipitation ratio(R_{S})	$\frac{\text{Jun-Aug precipitation}}{\text{Total precipitation}}$
Field	Intra-field	First and second empirical orthogonal function of precipitation field ($\mathrm{EOF}_{1/2}$)	Leading orthonormal eigenvectors of precipitation correlation matrix
	Inter-field	Applicability of $F^*_{\mathbf{X}}$ and $F^*_{\mathbf{Y}}$ for mapping $\mathbf{S_Y}$ to $\mathbf{Y}$, $\mathbf{S_X}$ to $\mathbf{X}$ or $G(\mathbf{X})$	$r\big(F^*_{\mathbf{X}}(\mathbf{S_Y}),\mathbf{Y}\big)$, $r\big(F^*_{\mathbf{X}}(\mathbf{S_X}),\mathbf{X}\big)$, $r\big(F^*_{\mathbf{X}}(\mathbf{S_X}),G(\mathbf{X})\big)$ $r\big(F^*_{\mathbf{Y}}(\mathbf{S_Y}),\mathbf{Y}\big)$, $r\big(F^*_{\mathbf{Y}}(\mathbf{S_X}),\mathbf{X}\big)$, $r\big(F^*_{\mathbf{Y}}(\mathbf{S_X}),G(\mathbf{X})\big)$

precipitation. We assess the significance of bias correction improvements using the following bootstrap test: We first generate 100 bootstrap samples of precipitation observation and simulation time series before and after correction. Thereafter, we calculate the ratio that the target index after bias correction better matches that of observation. The confidence interval is thereafter determined using a percentile method. All tests are one-tailed and use a confidence level of 99%. We further apply the spatial correlation (r) and spatial average root mean square error (RMSE) between observation and simulation for these indices to roughly summarize the climate simulation performance before and after correction.

$$r = \frac{\sum_{i,j}(\zeta^{\mathbf{X}}_{i,j} - \overline{\zeta^{\mathbf{X}}})(\zeta^{\mathbf{Y}}_{i,j} - \overline{\zeta^{\mathbf{Y}}})}{\sqrt{\sum_{i,j}(\zeta^{\mathbf{X}}_{i,j} - \overline{\zeta^{\mathbf{X}}})^2(\zeta^{\mathbf{Y}}_{i,j} - \overline{\zeta^{\mathbf{Y}}})^2}} \tag{6}$$

$$\mathrm{RMSE} = \sqrt{\frac{1}{N}\sum_{i,j}(\zeta^{\mathbf{X}}_{i,j} - \zeta^{\mathbf{Y}}_{i,j})^2} \tag{7}$$

Here $\zeta^{\mathbf{X}}_{i,j}$ and $\zeta^{\mathbf{Y}}_{i,j}$ are the considered indices for simulation and observation at geogrid (i,j), $\overline{\zeta^{\mathbf{X}}}$ and $\overline{\zeta^{\mathbf{Y}}}$ are the spatial average of the statistics, N is the total number of geogrids.

For field scale assessment, we consider the linear spatial structure of the precipitation field revealed by its leading two empirical orthogonal function ($\mathrm{EOF}_{1,2}$). Also, we consider the inter-field coherency between precipitation and resolved dynamics by evaluating how the simulation-based and observation-based statistical downscaling model ($F^*_{\mathbf{X}}$ and $F^*_{\mathbf{Y}}$) works for the observation and simulation data. We illustrate the rationale for these evaluations in the following section.

4 Bias correction results

4.1 General performance

We evaluate the RADA methodology by examining if the distribution of the precipitation indices better match observations after bias correction. Evaluation results for the test set (1995-2004) are presented in Fig. 3-8. Each sub-figure here shows the spatial maps of a considered precipitation index for observations (left), CESM2 historical simulations before (middle) and after (right) bias correction.

In general, the RADA methodology demonstrates favorable performance by faithfully representing the spatial variability of precipitation distribution, improving the spatial correlation, and reducing the spatial average RMSE between observations and simulations for all the considered grid-scale indices (Fig. 3-6). We achieve significant skill improvements for a broad range of regions (stippled grids on the bias corrected maps), while the limited regions show significant skill drop (stippled grids on the uncorrected maps) for some low-precipitation related indices are mostly from mountain areas, suggesting the need for dedicated effort in modeling orographic effect in future development of our approach. Regarding the field-scale assessments, our method better simulates the linear spatial structure of the precipitation field (Fig. 7), and maintains the coherency between precipitation and the resolved dynamics (Fig. 8).

4.2 Moments

For moment based evaluations (Fig. 3), the improvements are reflected in the following four aspects. First, we obtain considerable improvements for the western mountain regions, especially for the Sierra Nevada, where the orographic lifting and shadowing impacts from the narrow mountain strips pose notorious difficulty for GCM simulations (Kapnick et al., 2018; Gershunov et al., 2019). Second, localized high precipitation variability incubated by peculiar geographical conditions can be well reproduced, such as for Southern California Bight. Third, the bias correction results better represent the intense and highly-variate coastal precipitation along the Gulf of Mexico, and alleviate the overestimation along the eastern coast. Finally, the bias correction results better match observations regarding the inland precipitation distribution.

4.3 Quantile, frequency, and intensity

For quantile, frequency, and intensity based evaluations (Fig. 4 and 5), we significantly alleviate the over estimation of low precipitation events for the Northern Great Plains, the Midwest, and the Southeast (Fig. 4a). Also, we significantly draw down the precipitation frequency estimation to better match observations for most regions (Fig. 4d). Exceptions are for mountain regions: our model tends to exacerbate the overestimation of 33% quantile for part of the Appalachian Mountain Range (Fig. 4a), while excessively eliminate certain amount of precipitation events for part of the Rocky Mountain range (Fig. 4a). These deficiencies may result from sharing feature-learning convolution kernels with regions of distinct precipitation orographical impacts.

Another favorable aspect of the RADA approach shown here is that, we obtain considerable improvement in simulating precipitation extremes, as reflected in the 99% quantile (Fig. 4c), 1-day maximum (Fig. 5b), 3-day maximum (Fig. 5c), and 5-day maximum (Fig. 5d) estimation maps. The improvements are particularly obvious for the west coast and the east north central regions. We can largely attribute this improvement to the following two reasons: first, although extreme precipitations are rare events locally, they are ubiquitous as viewed from a broader, i.e., continental, spatial scope. By modeling the continental precipitation field using CNNs, we obtain large sample diversity of extreme events. Second, while most existing climate-related machine learning methods apply maximum likelihood objective, which work poorly for modeling the tail of the dis-

tribution for the target variable (Van Horn & Perona, 2017; Pan, 2019), we apply the adversarial learning objective, encouraging the model to faithfully generate extremes as revealed by the observations.

4.4 Seasonality

In terms of seasonality (Fig. 6), winter precipitation variability in CONUS is largely dominated by extratropical cyclone related storm tracks. The cyclone-related precipitation can be enhanced or suppressed as the atmospheric flows encounter the orography. The bias correction results better represent the spatial variability of winter precipitation ratio for the orographical complicated regions, such as the western mountain regions (Fig. 6a). Also, we improve the representation of the dry winter climate for the Northern Rockies and plains (Fig. 6a). For summer precipitation (Fig. 6b), improvements are reflected in better representing the spatial variability of precipitation for the North American Monsoon in the southwest, coastal landing of tropical cyclones for the Gulf of Mexico and southeast coast. Furthermore, we also enhance the summer precipitation ratio to better match observations for the great plain.

4.5 Spatial Consistency

Regarding the spatial consistency of the precipitation estimation, we draw the first and second leading EOFs of the observed, simulated, and bias-corrected daily precipitation fields (Fig. 7). The EOFs represent the spatial loading of the leading principal components (PCs) that account for most precipitation variability. Therefore, these EOFs could roughly tell the linear spatial structure of the precipitation field. For EOF_1 (Fig. 7a), the bias correction result agrees better with observations, with a spatial correlation coefficient improved from 0.85 to 0.93, and the spatial RMSE dropped from 2.1×10^{-2} to $1.3{\times}10^{-2}$, suggesting that the leading mode of precipitation spatial variability can be better revealed using our approach. Besides, we lowered the ratio of explained variance of PC_1 from 2.22% to 1.51%, which better matches observation (1.29%). For EOF_2 (Fig. 7b), while there is a considerable discrepancy among the maps, in particular over the Western U.S., the bias correction results still agree better with the observation, especially for the Southeast. Bias corrected results achieve a spatial correlation of 0.57 regarding PC_2 loading, as compared to 0.15 in the original CESM2 simulation. These results suggest that the RADA methodology can maintain, and even improve, the spatial consistency of the target variable.

4.6 Inter-field correlation

Considering the inter-field correlation between precipitation and the resolved dynamics, we evaluate how the simulation-based and observation-based statistical models $F^*_{\mathbf{X}}$ and $F^*_{\mathbf{Y}}$) work for the observation and simulation data by calculating the r skill of these two models (Fig. 8). Conventionally, we consider GCM biases at a single variable level, the assessments here examine GCM biases at a functional relationship level.

For the simulation-based downscaling results (Fig. 8a), $F^*_{\mathbf{X}}$, which is trained using CESM2 historical simulation data, works particularly well for estimating CESM2 simulated precipitation using the simulated dynamical field information, achieving a spatial average r skill score of 0.89 during test (Fig. 8a middle, $r\big(F^*_{\mathbf{X}}(\mathbf{S_X}), \mathbf{X}\big)$). However, this GCM revealed inter-field relationship works far worse when applied to observations, with the average r skill score dropped to 0.42 (Fig. 8a left, $r\big(F^*_{\mathbf{X}}(\mathbf{S_Y}), \mathbf{Y}\big)$). This drop of skill can result from the following two reasons, first, the GCM imposes an overly stringent constraint on simulated precipitation variability; second, the downscaling relationship revealed the GCM has non-linear biases.

We dissect the impacts from both sides by examining the observation-based downscaling results (Fig. 8b). The impact of the first aspect (over stringency) is reflected in the fact that, $F^*_{\mathbf{Y}}$, trained using historical observational data, can not pose as stringent a constraint on observed precipitation (Fig. 8b left, $r\big(F^*_{\mathbf{Y}}(\mathbf{S_Y}), \mathbf{Y}\big)$) as $F^*_{\mathbf{X}}$ when applied to simulation data (Fig. 8a middle, $r\big(F^*_{\mathbf{X}}(\mathbf{S_X}), \mathbf{X}\big)$). In other words, the GCM underestimates the conditional variability of the parameterized variable given the resolved dynamics. The impact of the second aspect (non-linear bias) is reflected in the fact that, $F^*_{\mathbf{Y}}$ achieves an overall higher r skill score for estimating the observed precipitation using the dynamical field information (Fig. 8b left, $r\big(F^*_{\mathbf{Y}}(\mathbf{S_Y}), \mathbf{Y}\big)$), as compared to $F^*_{\mathbf{X}}$ when applied to observations (Fig. 8a left, $r\big(F^*_{\mathbf{X}}(\mathbf{S_Y}), \mathbf{Y}\big)$).

How are these two aspects of deficiencies reflected in the RADA bias correction results? First, as we apply $F^*_{\mathbf{X}}$ to estimate the bias corrected precipitation (Fig. 8a right, $r\big(F^*_{\mathbf{X}}(\mathbf{S_X}), G(\mathbf{X})\big)$), we obtain lower r skill compared to the estimation of the uncorrected precipitation (Fig. 8a middle, $r\big(F^*_{\mathbf{X}}(\mathbf{S_X}), \mathbf{X}\big)$), which is more consistent with the observation-based result (Fig. 8a left, $r\big(F^*_{\mathbf{X}}(\mathbf{S_Y}), \mathbf{Y}\big)$). This suggests that we may alleviate the deficiency in CESM2 precipitation estimation resulting from either over-stringency or non-linear bias. Second, $F^*_{\mathbf{Y}}$ obtains better applicability for the bias correction result (Fig. 8b right, $r\big(F^*_{\mathbf{Y}}(\mathbf{S_X}), G(\mathbf{X})\big)$), compared to its applicability for the original CESM2 precipitation estimation (Fig. 8b middle, $r\big(F^*_{\mathbf{Y}}(\mathbf{S_X}), \mathbf{X}\big)$). On one hand, this confirm that we alleviate the non-linear bias in estimating precipitation using the RADA methodology; on the other hand, since we still achieve considerable higher r skill for using $F^*_{\mathbf{Y}}$ to estimate the bias correction precipitation (Fig. 8b right, $r\big(F^*_{\mathbf{Y}}(\mathbf{S_X}), G(\mathbf{X})\big)$), compared to estimating the observed precipitation (Fig. 8b left, $r\big(F^*_{\mathbf{Y}}(\mathbf{S_Y}), \mathbf{Y}\big)$), the over stringency problem is not fully resolved by this deterministic bias correction approach. An implication here is that we may need to inject random noise into the bias corrector for probabilistic estimation of the unresolved precipitation processes, as is explored in stochastic parameterization practices (Berner et al., 2017). We revisit this issue in Sec. 8.2.1.

5 Ablation analysis

We have introduced three regularizers to enhance adversarial learning of GCM biases, namely, cycle consistency (Sec. 2.2.2), dynamical consistency (Sec. 2.2.3), and dynamical dependency (Sec. 2.2.4). Here, we quantify the contribution from each regularizer or their combinations using an ablation analysis method: we monitor the change of bias correction performance by systematically removing the regularizers in the RADA network architecture. The combinations of these three regularizers consist 7 GAN-based bias corrector baselines.

We show the bias correction results for each of the baseline models in Fig. S1-S7 in the supporting information. Each figure there draws the spatial maps of all the considered precipitation indices for observations and simulations before and after bias correction. To compare models' performances, Fig. 9 draws models' relative spatial correlation skills: for each model and each considered precipitation distribution characteristics, we first calculate the spatial correlation between the observation-revealed precipitation indices and simulation-revealed precipitation indices, thereafter, we re-scale the models' correlation skills to the range of [0, 1] by subtracting the minimum correlation skill achieved by the 9 considered precipitation simulations (CESM2 original simulation, RADA bias correction, and 7 GAN-based bias correction), and dividing the result by the difference between the maximum and minimum correlation skill achieved by these models. The skills of CESM2 original simulation (grey dashed) and RADA corrected simulation (black solid) are plotted as benchmarks.

The key findings are summarized here. Applying unconstrained GAN for bias correction yields poor performance regarding most of the considered precipitation distribution characteristics (Fig. 9a). This is because, GANs are trained to produce individ-

ual trust-worthy samples, not accurate probability distribution estimations (Goodfellow, 2016). The overall performance is generally improved as more regularizers are included to constrain the bias corrector (Fig. 9b-g), although the inclusion of a new regularizer might hamper the performance for certain aspects. The RADA bias corrector containing all three regularizers achieves overall the best performance compared to the rest GAN-based models. These evidences empirically confirm the arguments made in Sec. 2.2.1, and justify the contribution of the proposed regularizers.

6 Comparison study

In this section, we compare the RADA methodology with widely-applied univariate and multivariate bias correction approaches. The first approach is *quantile mapping*, which is a univariate correction technique that maps quantiles of historical climate simulations to quantiles of corresponding climate observations (Michelangeli et al., 2009; Mamalakis et al., 2017):

$$x_c = \mathrm{CDF}_{\mathbf{Y}}^{-1}\big(\mathrm{CDF}_{\mathbf{X}}(x)\big) \tag{8}$$

Here x and x_c are the grid-scale target variable simulation before and after bias correction, $\mathrm{CDF}_{\mathbf{Y}}^{-1}$ is the inverse of the empirical cumulative distribution function of the observation, $\mathrm{CDF}_{\mathbf{X}}$ is the empirical cumulative distribution function of the original simulation. Both $\mathrm{CDF}_{\mathbf{Y}}^{-1}$ and $\mathrm{CDF}_{\mathbf{X}}$ are built on the training set data as defined in Sec. 3.2.3. Model performance is evaluated on the test set. The implementation details are described in the supporting information.

The *quantile mapping* approach neglects the spatial consistency of the target variable in its correction. Regarding this deficiency, many multivariate bias correction methods have been developed, although the robustness and benefits of these multivariate methods are frequently questioned (Maraun & Widmann, 2018; Räty et al., 2018), and remain to be rigorously tested (Maraun, 2016; François et al., 2020). Here we consider the *Multivariate Bias Correction with N-dimensional probability density function transform* (MBCn, Pitie et al. 2005; Cannon 2018) approach to correct precipitation projection biases while maintaining the spatial consistency. MBCn is adopted for the following three reasons: First, MBCn is claimed to achieve competitive performance compared to univariate or other multivariate bias correction approaches (Cannon, 2018; François et al., 2020). Second, the computation cost for scaling up MBCn to high dimensional data is relatively low. Third, we do not need to pre-assume the parametric distribution form of the considered climate variable.

MBCn maps a multivariate source distribution to a same-dimensional target distribution by iteratively applying the following three steps. First, rotate the multivariate source distribution and target distribution with a same uniformly distributed random orthogonal matrix. Second, apply *quantile mapping* to match the source distribution with the target distribution for each of the rotated dimensions. Third, apply the inverse rotation matrix to yield source values for the next iteration. By the end of each iteration, an *energy distance* function (Rizzo & Székely, 2016) is applied to measure the distance between corrected source distribution and target distribution. We consider two strategies for stopping the iterative bias correction process: the first strategy, following the setting in Cannon (2018), is to stop the iteration as the *energy distance* function evaluated for the training set converges; the second strategy, as advocated in the discussion section of Cannon (2018), is to use early stopping (Prechelt, 1998): we stop the iteration as the *energy distance* function evaluated for the validation set stops decreasing. We evaluate the model performance using the test set data. The implementations can be found in the supporting information. More details can be found in Cannon (2018) and François et al. (2020).

The comparison results are presented in a similar manner as Sec. 5. We show the bias correction results for *quantile mapping* and MBCn in supporting information Fig. S8

(*quantile mapping*) and S9-S10 (MBCn without/with early stopping). Each figure draws the spatial maps of all the considered precipitation indices for observations and simulations before and after bias correction. Figure 10 draws models' relative spatial correlation skills (see Sec. 5 for computation details).

The *quantile mapping* approach (Fig. 10a) obtains good performance for correcting grid-scale precipitation distribution characteristics, slightly surpassing the RADA approach regarding some of the considered indices (μ, σ, $Q_{66\%}$, $Q_{99\%}$, and Int). These are reasonable results as we empirically align the simulated precipitation distribution to match observed precipitation distribution for each grid cell. Meanwhile, the RADA approach demonstrates advantage for better matching observations regarding the higher-order moments (Skew and Kurt), $Q_{33\%}$, the probability of precipitation, the daily maximum precipitation, the seasonal precipitation ratio, and all the field-scale precipitation characteristics. For grid-scale assessments, the disadvantage of *quantile mapping* here may due to the fact that these statistics are sensitive to sampling variance, requiring more samples to build empirical CDFs that better characterize these statistics, while the advantage of RADA is achieved by generalizing from limited available data using deep neural networks. For field-scale assessments, the disadvantage of *quantile mapping* is due to the fact that it does not explicitly take into consideration of spatiotemporal consistency or inter-field correlation, while the RADA is designed to overcome these deficiencies.

The MBCn approach (Fig. 10b-c red) obtains relatively lower skill compared to either the *quantile mapping* approach or the RADA approach. Even worse, many of the statistical indices, after MBCn bias correction, match less well with observations. This degradation of skill is particularly obvious if the early stopping strategy is not adopted (Fig. 10b). We provide the following explanations for these phenomena. First, most of the reported implementations of MBCn apply cross-validation evaluation (Cannon, 2018; François et al., 2020), which tend to yield misleadingly promising performance, see Maraun et al. (2017) and Maraun & Widmann (2018) for theoretical and empirical proofs. As we evaluate the MBCn approach using a hold-out test set, we find the iterative bias correction strategy in MBCn generalizes poorly, as compared to either the straightforward, one-step *quantile mapping* approach, or the sophisticated, but well regularized RADA approach. Second, in each iteration, MBCn uses a random orthogonal matrix to partially de-correlate the precipitation field data, and carry out bias correction on the basis of the orthogonal matrix. This linear assumption may not work well for the highly variate precipitation field data. Overall, the results here suggest the difficulty for extending univariate bias correction to multivariate cases, and highlight the contribution of the RADA methodology.

Finally, it is worth noticing that, many recent works have tried to correct climate model biases conditioned on model resolved dynamics (Wetterhall et al., 2012; Bellprat et al., 2013; Addor et al., 2016), which echoes the idea of applying resolved dynamics to regularize the bias correction in the RADA methodology. However, these existing works often overly simplify the dynamical states conditioned on which to correct model biases. For instance, Manzanas & Gutiérrez (2019) showed that, conditioning the bias corrector on large scale circulation patterns, such as El Niño/Southern Oscillation (Manzanas & Gutiérrez, 2019), enhances model's seasonal forecasting capability. The RADA methodology suggests a potential direction for correcting climate model biases conditioned on more detailed dynamical state information.

7 Perceptual evaluation

The RADA methodology, derived from the idea of *adversarial learning*, builds an evolving game between the neural network parameterized bias detector and bias corrector under cycle-consistent statistical and dynamical constraints. The overall loss func-

tion (Eq. 5) does not directly inform the model performance or when to stop the training. In many GAN applications, the training is stopped when there is no perceptual improvement of the generated samples (Salimans et al., 2016). Here, we evaluate the perceptual performance of the RADA methodology. We empirically prove that, compared to the judgement made by the neural network parameterized bias detector, the perceptual judgement made by human beings can be easily fooled in our problem setting, yielding less optimal bias correction performance.

We consider a binary distinction of climate observation samples and simulation samples, judged by a human being test taker and a separately trained deep neural network. This problem formulation is similar to the climatic Turing test proposed by Palmer (2016). The deep neural network applied here has same architecture as the RADA discriminative neural network, but unlike the setting in Wasserstein GAN, the weights are not clipped to fully explore its discrimination power. Both the human being and the deep neural network are trained to distinguish historical climate observation samples and simulation samples, and are tested to make distinctions for a holdout test set. We compare the human being and the deep neural network performance for the distinction task before and after RADA bias correction. Results are shown in Fig. 11.

The top of Fig. 11 shows randomly selected samples of precipitation observation maps (first row) and the CESM2 precipitation simulation maps before (second row) and after (third row) bias correction. The simulations do not match the observations, as the freely evolving historical climate simulations do not follow the evolution of historical climate variability. Although unpaired, we can still easily distinguish the observations (first row) and the original simulations (second row): the observations are of higher spatial variability, and are featured by well-pronounced orographical impact; the simulations are of lower spatial variability, and are featured by well-expanded drizzles. The RADA bias correction results (third row) largely overcome the perceptual deficiencies, while still matching the spatial distribution pattern of the original simulations.

The bottom of Fig. 11 summarizes the performance of the human being test taker (top) and the deep neural network (bottom) for distinguishing observation samples and simulation samples before (left) and after (right) bias correction. Here, TP, FP, TN, and FN are true positive rate, false positive rate, true negative rate, and false negative rate, respectively. Before bias correction, both the human being test taker and the deep neural network can well distinguish the observation samples and the simulation samples. While the human being test taker misclassifies 5% of the samples, the accuracy of the deep neural network is nearly perfect. After bias correction, the human being test taker assigns 67.92% of simulation samples to observations, while the deep neural network shows a large advantage for distinguishing the observation and simulation samples. These results suggest that, first, the perceptual judgement made by human beings is not as accurate as the judgement made by the discriminative deep neural network. In the current problem setting and many other physical applications, we should not rely purely upon perceptual judgement to evaluate the model performance, or to determine the training stopping criteria. Second, since a separately trained deep neural network can still distinguish the observation samples and the simulation samples with moderate accuracy, the current bias correction model may not have fully exploited the bias information in the data. We discuss the limitations of the model, and suggest potential directions for improvements in Sec. 8.2.

8 Conclusion and future work

8.1 Contributions

The accuracy of climate projection is continuously marred by biases of climate models, due to their simplification or misrepresentation of unresolved climate processes. The

community has reached a consensus that, to significantly improve climate projection accuracy in the next-generation climate models, we should leverage the information hidden in multi-resolution simulations and multi-source observations, using the powerful tools of machine learning (Schneider et al., 2017; Gentine et al., 2018). Current endeavors along this direction mainly focus on learning data-driven parameterization schemes from high-resolution simulations, either deterministically (Rasp et al., 2018; Yuval & O'Gorman, 2020) or probabilistically (Schneider et al., 2020; Gagne et al., 2020).

Despite these efforts, climate models equipped with enhanced parameterization schemes (either conceptual based, or machine learning based) may still disagree with observations in many aspects, reflecting the gap between parameterization development and application, and highlighting the sophisticated structure of climate model biases. These biases can not be readily revealed by contrasting historical climate simulation and observation time series, as the freely evolving historical climate simulations do not follow the evolution of actually observed historical climate variability. To identify and alleviate these biases, we may either carry out costly process-oriented diagnosis, or adjust model output distribution toward observations regardless of physical justifications. It remains challenging to efficiently apply the simulation-observation "disagreement" information to diagnose and improve climate models.

In this study, we develop the Regularized Adversarial Domain Adaptation (RADA) methodology that learns to identify and correct climate projection biases using unpaired climate simulation and observation data. We are inspired by the fact that, climate experts can easily distinguish maps of observations and model simulations, even though they represent different climate states (Palmer, 2016). As we apply a deep neural network for this observation-simulation distinction task, the evidences based on which this network derives its judgement roughly tell where the model bias lies, which can be inversely applied to train a domain adaptation network to have simulations less distinguishable from observations. Eventually, this may lead us to the ideal of *digital twin* (Bauer et al., 2021) for developing climate models.

The *adversarial learning* process can be highly unconstrained, yielding superficially authentic yet physically unreasonable results. We turn the three requirements that Ehret et al. (2012) conceived for a "perfect" bias corrector into regularizers to support the *adversarial learning* of climate model biases. Specifically, we include cycle consistency regularization to encourage model to produce identical simulations as observations under same resolved dynamical states; we include dynamical consistency regularization to ensure spatiotemporal consistency as well as inter-field correlations in bias correction; we make the bias corrector dynamical dependent to discriminate between different dynamical conditions.

We apply this RADA methodology for correcting the Community Earth System Model version 2 daily precipitation projection over the Contiguous United States. Results show that our methodology can correct all the considered moments of daily precipitation at approximately 1° resolution, ensure spatiotemporal consistency and inter-field correlations, and discriminate between different dynamical states. We apply an ablation study to justify the contribution of the introduced regularizers. Compared to existing univariate and multivariate bias correction approach, our methodology can well correct all the considered statistics at grid scale, and perform better in maintaining intra-field and inter-field consistency.

The key message we want to deliver is that, we should *learn* from big data of climate observations and simulations to criticize and improve the ever-complicated climate models. Logically, sophisticated climate models should come with equally sophisticated diagnosis tools (Hofstadter, 1979), which could be built upon our methodology. We summarize three of our key contributions as follows:

1. We develop a powerful and efficient paradigm for learning climate projection biases using unpaired climate simulation and observation data.
2. We introduce useful regularization approaches to support physically consistent *adversarial learning* of climate projection biases. New regularizers can be more easily included following the strategies developed here.
3. We describe comprehensive training and evaluation details for implementing and assessing the proposed data-driven bias correction methodology, demonstrating the advantage of our approach over existing univariate or multivariate bias correction methods.

8.2 Limitations and future work

We have developed an *adversarial learning* based data-driven climate model bias corrector (RADA), equipped with three regularizers targeted toward the three requirements that Ehret et al. (2012) conceived for a "perfect" bias correction algorithm. Here, we highlight four limitations of the current RADA methodology, and discuss our future work directions.

8.2.1 Scalability

The current RADA methodology is applied to correct daily precipitation projection at 1° resolution. In order to make this methodology applicable for GCMs with increasingly high resolutions, we should address the following two problems: first, how to scale the learning algorithm to high spatiotemporal resolution cases; second, how to include stochastic component to account for the inherent uncertainty in parameterizing the unresolved processes (Berner et al., 2017). Below, we discuss the challenges and possible solutions of these two problems.

Since the development of the first GAN model (Goodfellow et al., 2014), many works have explored the possibility of scaling *adversarial learning* to large models and datasets, achieving consistent progresses regarding training stability, computation efficiency, and output quality (Radford et al., 2015; Kurakin et al., 2016; Karras et al., 2017, 2019). In particular, Karras et al. (2017) showed that, starting from a low resolution, as we progressively add new layers to refine the model output details, we can achieve robust, high-resolution results in *adversarial learning*. In our future work, we plan to apply this idea to extend the RADA methodology from moderate resolution to high resolution.

While it is relatively straightforward to follow existing works to scale the learning machine to high resolution cases, we should notice the physical limitation here: as the GCM resolution is increased, there is no clear scale separation between resolved dynamics and parameterized physics (Gerard, 2007). In this case, the resolved dynamics can not support a strict one-to-one mapping between observations and simulations. This partially explains why the cycle consistency regularization (Sec. 2.2.2) does not significantly enhance bias correction performance (Fig. 9b). To address this problem, we should include stochastic component to account for the inherent uncertainty in parameterizing the unresolved processes (Berner et al., 2017). Similar issue has been studied in the machine learning literature (Almahairi et al., 2018; Park et al., 2020). Instead of learning strict one-to-one mapping between domains, these methods are designed to learn probabilistic, many-to-many mappings. In particular, by adding auxiliary latent variables to the cycle-consistency GAN model, Almahairi et al. (2018) showed that we can learn mappings that capture diversity of the outputs in domain adaptation. In our future work, we plan to explore similar idea to learn stochastic bias correction for high dimensional cases.

8.2.2 Explainability

A unique feature of the RADA methodology is that, we do not pre-assume where the GCM biases are, and apply universal function approximators (deep neural nets, Leshno et al. 1993) to identify (via D) and correct (via G) these biases. Although this setting may potentially allow us to identify and correct arbitrary GCM biases, the spatiotemporal characteristics of the GCM biases and their dependency on the GCM resolved dynamics remain vague. To apply this modeling framework for climate studies, the neural network should provide human-understandable justifications for its outputs, and help model developers to diagnose and improve GCMs. Several neural network interpretability techniques, including *saliency maps* (Simonyan et al., 2013), *occlusion sensitivity analysis* (Zeiler & Fergus, 2014), *backward optimization* (Olah et al., 2017) and *layerwise relevance propagation* (Bach et al., 2015; Toms et al., 2020), could be applied to verify if the RADA methodology identifies meaningful model biases, enhance our understanding of model deficiencies, and support model improvement.

8.2.3 Applicability in a changing climate

We have trained the RADA model using historical climate simulation and observation data from 1950-1994, and test the bias correction performance using a hold-out test set, covering 1995-2004. The results suggest that the RADA methodology applies well for a "future", changing scenario. Meanwhile, the evaluation here does not guarantee that the bias corrector trained using historical data can extrapolate well in a severely changed climate, such as the climate projections forced by high greenhouse gas emission scenarios. On the one hand, we should strictly exam the bias correction performance for different climate periods; on the other hand, we should apply the detailed bias information offered by the RADA methodology to diagnose and improve the GCMs, translating the black-box model diagnosed bias information into robust knowledge encoded in climate models. The following section offers a potential direction to achieve this goal.

8.2.4 Feedback effects

The three regularizers in the RADA methodology target toward the three requirements that Ehret et al. (2012) conceived for a "perfect" bias correction algorithm. So far, we have not explicitly considered the feedback effect associated with GCM parameterization biases, which consists the last requirement from Ehret et al. (2012), as well as the most difficult challenge in correcting climate projection biases.

There are potentially two directions toward tackling the feedback effects from a bias correction perspective, one is to couple the bias corrector with dynamical simulations, the other is to iteratively correct the parameterization biases and alleviate their impacts on model resolved dynamics.

The latter direction is more feasible as it poses lower requirement on the spatiotemporal resolution of the bias corrector, and lighter burden on model development. Provided that the bias corrector can pinpoint detailed spatiotemporal bias information without costly initialization and long-term running of climate models, we could obtain sufficient guidance for calibrating and improving climate models (Hourdin et al., 2017; Gong et al., 2016; Anderson & Lucas, 2018; Rasp et al., 2018; Yuval & O'Gorman, 2020). By iteratively training and applying this bias corrector to overcome the parameterization biases, we may gradually alleviate their impacts on model dynamics, therefore resolve the feedback impacts of parameterization biases.

To support the blueprint drawn above, we should test if the bias corrector can offer detailed spatiotemporal bias information. A perfect test bed is weather forecast postprocessing. Historically, postprocessing in weather forecast and bias correction in climate

projection are considered as two disciplines (Maraun, 2016), although they result from similar model biases.

The barrier that prevents us from carrying out a weather forecast postprocessing verification of our methodology is that, retrospective weather forecast experiments usually apply different GCM settings compared with climate projections, regarding the resolution, numerical solver, and parameterization choices. The community has realized the necessity for applying an integrated forecasting system across weather to seasonal scale. Here we advocate that the unification should extend to climate scale for better identification and correcting of forecasting model biases. Before this is carried out, our future works plan to test if the learned bias corrector can enhance weather to seasonal forecast in a semi-supervised learning manner, alleviating the sample limitation problem in learning forecasting biases.

References

Addor, N., Rohrer, M., Furrer, R., & Seibert, J. (2016). Propagation of biases in climate models from the synoptic to the regional scale: Implications for bias adjustment. *Journal of Geophysical Research: Atmospheres*, *121*(5), 2075–2089.

Almahairi, A., Rajeshwar, S., Sordoni, A., Bachman, P., & Courville, A. (2018). Augmented cyclegan: Learning many-to-many mappings from unpaired data. In *International conference on machine learning* (pp. 195–204).

Anderson, G. J., & Lucas, D. D. (2018). Machine learning predictions of a multiresolution climate model ensemble. *Geophysical Research Letters*, *45*(9), 4273–4280.

Arjovsky, M., Chintala, S., & Bottou, L. (2017). Wasserstein gan. *arXiv preprint arXiv:1701.07875*.

Bach, S., Binder, A., Montavon, G., Klauschen, F., Müller, K.-R., & Samek, W. (2015). On pixel-wise explanations for non-linear classifier decisions by layer-wise relevance propagation. *PloS one*, *10*(7), e0130140.

Baño-Medina, J. L., García Manzanas, R., Gutiérrez Llorente, J. M., et al. (2020). Configuration and intercomparison of deep learning neural models for statistical downscaling.

Barnes, E. A., Hurrell, J. W., Ebert-Uphoff, I., Anderson, C., & Anderson, D. (2019). Viewing forced climate patterns through an ai lens. *Geophysical Research Letters*, *46*(22), 13389–13398.

Bauer, P., Stevens, B., & Hazeleger, W. (2021). A digital twin of earth for the green transition. *Nature Climate Change*, *11*(2), 80–83.

Bellprat, O., Kotlarski, S., Lüthi, D., & Schär, C. (2013). Physical constraints for temperature biases in climate models. *Geophysical Research Letters*, *40*(15), 4042–4047.

Berner, J., Achatz, U., Batte, L., Bengtsson, L., De La Camara, A., Christensen, H. M., ... others (2017). Stochastic parameterization: Toward a new view of weather and climate models. *Bulletin of the American Meteorological Society*, *98*(3), 565–588.

Bottou, L. (2010). Large-scale machine learning with stochastic gradient descent. In *Proceedings of compstat'2010* (pp. 177–186). Springer.

Cannon, A. J. (2018). Multivariate quantile mapping bias correction: an n-dimensional probability density function transform for climate model simulations of multiple variables. *Climate dynamics*, *50*(1), 31–49.

Christensen, J. H., Boberg, F., Christensen, O. B., & Lucas-Picher, P. (2008). On the need for bias correction of regional climate change projections of temperature and precipitation. *Geophysical Research Letters*, *35*(20).

Cohen, J. P., Luck, M., & Honari, S. (2018). Distribution matching losses can hallucinate features in medical image translation. In *International conference on medi-*

cal image computing and computer-assisted intervention (pp. 529–536).

Danabasoglu, G., Lamarque, J.-F., Bacmeister, J., Bailey, D., DuVivier, A., Edwards, J., ... others (2020). The community earth system model version 2 (cesm2). *Journal of Advances in Modeling Earth Systems*, *12*(2), e2019MS001916.

Ehret, U., Zehe, E., Wulfmeyer, V., Warrach-Sagi, K., & Liebert, J. (2012). HESS Opinions" Should we apply bias correction to global and regional climate model data?". *Hydrology & Earth System Sciences*, *9*(4).

Eyring, V., Bony, S., Meehl, G. A., Senior, C. A., Stevens, B., Stouffer, R. J., & Taylor, K. E. (2016). Overview of the coupled model intercomparison project phase 6 (cmip6) experimental design and organization. *Geoscientific Model Development*, *9*(5), 1937–1958.

Flato, G., Marotzke, J., Abiodun, B., Braconnot, P., Chou, S. C., Collins, W., ... others (2014). Evaluation of climate models. In *Climate change 2013: the physical science basis. contribution of working group i to the fifth assessment report of the intergovernmental panel on climate change* (pp. 741–866). Cambridge University Press.

François, B., Vrac, M., Cannon, A. J., Robin, Y., & Allard, D. (2020). Multivariate bias corrections of climate simulations: which benefits for which losses? *Earth System Dynamics*, *11*(2), 537–562.

Gagne, D. J., Christensen, H. M., Subramanian, A. C., & Monahan, A. H. (2020). Machine learning for stochastic parameterization: Generative adversarial networks in the lorenz'96 model. *Journal of Advances in Modeling Earth Systems*, *12*(3), e2019MS001896.

Gentine, P., Pritchard, M., Rasp, S., Reinaudi, G., & Yacalis, G. (2018). Could machine learning break the convection parameterization deadlock? *Geophysical Research Letters*, *45*(11), 5742–5751.

Gerard, L. (2007). An integrated package for subgrid convection, clouds and precipitation compatible with meso-gamma scales. *Quarterly Journal of the Royal Meteorological Society: A journal of the atmospheric sciences, applied meteorology and physical oceanography*, *133*(624), 711–730.

Gershunov, A., Shulgina, T., Clemesha, R. E., Guirguis, K., Pierce, D. W., Dettinger, M. D., ... others (2019). Precipitation regime change in western north america: the role of atmospheric rivers. *Scientific reports*, *9*(1), 1–11.

Gong, W., Duan, Q., Li, J., Wang, C., Di, Z., Ye, A., ... Dai, Y. (2016). Multiobjective adaptive surrogate modeling-based optimization for parameter estimation of large, complex geophysical models. *Water Resources Research*, *52*(3), 1984–2008.

Goodfellow, I. (2016). Nips 2016 tutorial: Generative adversarial networks. *arXiv preprint arXiv:1701.00160*.

Goodfellow, I., Pouget-Abadie, J., Mirza, M., Xu, B., Warde-Farley, D., Ozair, S., ... Bengio, Y. (2014). Generative adversarial nets. In *Advances in neural information processing systems* (pp. 2672–2680).

He, K., Zhang, X., Ren, S., & Sun, J. (2016). Deep residual learning for image recognition. In *Proceedings of the ieee conference on computer vision and pattern recognition* (pp. 770–778).

Hofstadter, D. R. (1979). *Gödel, escher, bach*. Harvester press Hassocks.

Hourdin, F., Mauritsen, T., Gettelman, A., Golaz, J.-C., Balaji, V., Duan, Q., ... others (2017). The art and science of climate model tuning. *Bulletin of the American Meteorological Society*, *98*(3), 589–602.

Kapnick, S. B., Yang, X., Vecchi, G. A., Delworth, T. L., Gudgel, R., Malyshev, S., ... Margulis, S. A. (2018). Potential for western us seasonal snowpack prediction. *Proceedings of the National Academy of Sciences*, *115*(6), 1180–1185.

Karras, T., Aila, T., Laine, S., & Lehtinen, J. (2017). Progressive growing of gans for improved quality, stability, and variation. *arXiv preprint arXiv:1710.10196*.

Karras, T., Laine, S., & Aila, T. (2019). A style-based generator architecture for generative adversarial networks. In *Proceedings of the ieee/cvf conference on computer vision and pattern recognition* (pp. 4401–4410).

Kim, T., Cha, M., Kim, H., Lee, J. K., & Kim, J. (2017). Learning to discover cross-domain relations with generative adversarial networks. *arXiv preprint arXiv:1703.05192*.

Kingma, D. P., & Ba, J. (2014). Adam: A method for stochastic optimization. *arXiv preprint arXiv:1412.6980*.

Krizhevsky, A., Sutskever, I., & Hinton, G. E. (2012). Imagenet classification with deep convolutional neural networks. *Communications of the ACM*, *60*(6), 84–90.

Kurakin, A., Goodfellow, I., & Bengio, S. (2016). Adversarial machine learning at scale. *arXiv preprint arXiv:1611.01236*.

Kutz, J. N. (2017). Deep learning in fluid dynamics. *Journal of Fluid Mechanics*, *814*, 1–4.

LeCun, Y., Bengio, Y., et al. (1995). Convolutional networks for images, speech, and time series. *The handbook of brain theory and neural networks*, *3361*(10), 1995.

Leshno, M., Lin, V. Y., Pinkus, A., & Schocken, S. (1993). Multilayer feedforward networks with a nonpolynomial activation function can approximate any function. *Neural networks*, *6*(6), 861–867.

Li, H., Sheffield, J., & Wood, E. F. (2010). Bias correction of monthly precipitation and temperature fields from intergovernmental panel on climate change ar4 models using equidistant quantile matching. *Journal of Geophysical Research: Atmospheres*, *115*(D10).

Li, L., Zhang, L., Xia, J., Gippel, C. J., Wang, R., & Zeng, S. (2015). Implications of modelled climate and land cover changes on runoff in the middle route of the south to north water transfer project in china. *Water Resources Management*, *29*(8), 2563–2579.

Liu, M.-Y., Breuel, T., & Kautz, J. (2017). Unsupervised image-to-image translation networks. In *Proceedings of the 31st international conference on neural information processing systems* (pp. 700–708).

Ma, F., Ye, A., Deng, X., Zhou, Z., Liu, X., Duan, Q., ... Gong, W. (2016). Evaluating the skill of nmme seasonal precipitation ensemble predictions for 17 hydroclimatic regions in continental china. *International Journal of Climatology*, *36*(1), 132–144.

Ma, H.-Y., Xie, S., Klein, S., Williams, K., Boyle, J., Bony, S., ... others (2014). On the correspondence between mean forecast errors and climate errors in cmip5 models. *Journal of Climate*, *27*(4), 1781–1798.

Mamalakis, A., Langousis, A., Deidda, R., & Marrocu, M. (2017). A parametric approach for simultaneous bias correction and high-resolution downscaling of climate model rainfall. *Water Resources Research*, *53*(3), 2149–2170.

Manzanas, R., & Gutiérrez, J. M. (2019). Process-conditioned bias correction for seasonal forecasting: a case-study with enso in peru. *Climate Dynamics*, *52*(3), 1673–1683.

Maraun, D. (2013). Bias correction, quantile mapping, and downscaling: Revisiting the inflation issue. *Journal of Climate*, *26*(6), 2137–2143.

Maraun, D. (2016). Bias correcting climate change simulations-a critical review. *Current Climate Change Reports*, *2*(4), 211–220.

Maraun, D., Shepherd, T. G., Widmann, M., Zappa, G., Walton, D., Gutiérrez, J. M., ... others (2017). Towards process-informed bias correction of climate change simulations. *Nature Climate Change*, *7*(11), 764–773.

Maraun, D., & Widmann, M. (2018). Cross-validation of bias-corrected climate simulations is misleading. *Hydrology and Earth System Sciences*, *22*(9), 4867–4873.

Marvel, K., & Bonfils, C. (2013). Identifying external influences on global precipitation. *Proceedings of the National Academy of Sciences*, *110*(48), 19301–19306.

Miao, Q., Pan, B., Wang, H., Hsu, K., & Sorooshian, S. (2019). Improving monsoon precipitation prediction using combined convolutional and long short term memory neural network. *Water*, *11*(5), 977.

Michelangeli, P.-A., Vrac, M., & Loukos, H. (2009). Probabilistic downscaling approaches: Application to wind cumulative distribution functions. *Geophysical Research Letters*, *36*(11).

Mills, K., Spanner, M., & Tamblyn, I. (2017). Deep learning and the schrödinger equation. *Physical Review A*, *96*(4), 042113.

Olah, C., Mordvintsev, A., & Schubert, L. (2017). Feature visualization. *Distill*, *2*(11), e7.

Palmer, T. (2016). A personal perspective on modelling the climate system. *Proceedings of the Royal Society A: Mathematical, Physical and Engineering Sciences*, *472*(2188), 20150772.

Pan, B. (2019). *Advancing precipitation prediction using a composite of models and data* (Unpublished doctoral dissertation). UC Irvine.

Pan, B., Anderson, G. J., Goncalves, A., Lucas, D. D., Bonfils, C. J., & Lee, J. (2020). Improving seasonal forecast using probabilistic deep learning. *arXiv preprint arXiv:2010.14610*.

Pan, B., Anderson, G. J., Lucas, D. D., Goncalves, A., Bonfils, C., Lee, J., & Tian, Y. (2020). Identifying and correcting climate projection biases using artificial intelligence. In *Agu fall meeting 2020.*

Pan, B., Hsu, K., AghaKouchak, A., & Sorooshian, S. (2019). Improving precipitation estimation using convolutional neural network. *Water Resources Research*, *55*(3), 2301–2321.

Pan, B., Hsu, K., AghaKouchak, A., Sorooshian, S., & Higgins, W. (2019). Precipitation prediction skill for the west coast united states: From short to extended range. *Journal of Climate*, *32*(1), 161–182.

Park, T., Efros, A. A., Zhang, R., & Zhu, J.-Y. (2020). Contrastive learning for unpaired image-to-image translation. In *European conference on computer vision* (pp. 319–345).

Phillips, T. J., Potter, G. L., Williamson, D. L., Cederwall, R. T., Boyle, J. S., Fiorino, M., ... Yio, J. J. (2004). Evaluating parameterizations in general circulation models: Climate simulation meets weather prediction. *Bulletin of the American Meteorological Society*, *85*(12), 1903–1916.

Piani, C., Weedon, G., Best, M., Gomes, S., Viterbo, P., Hagemann, S., & Haerter, J. (2010). Statistical bias correction of global simulated daily precipitation and temperature for the application of hydrological models. *Journal of hydrology*, *395*(3-4), 199–215.

Pitie, F., Kokaram, A. C., & Dahyot, R. (2005). N-dimensional probability density function transfer and its application to color transfer. In *Tenth ieee international conference on computer vision (iccv'05) volume 1* (Vol. 2, pp. 1434–1439).

Poli, P., Hersbach, H., Dee, D. P., Berrisford, P., Simmons, A. J., Vitart, F., ... others (2016). Era-20c: An atmospheric reanalysis of the twentieth century. *Journal of Climate*, *29*(11), 4083–4097.

Prechelt, L. (1998). Automatic early stopping using cross validation: quantifying the criteria. *Neural Networks*, *11*(4), 761–767.

Radford, A., Metz, L., & Chintala, S. (2015). Unsupervised representation learning with deep convolutional generative adversarial networks. *arXiv preprint arXiv:1511.06434*.

Rasp, S., & Lerch, S. (2018). Neural networks for postprocessing ensemble weather forecasts. *Monthly Weather Review*, *146*(11), 3885–3900.

Rasp, S., Pritchard, M. S., & Gentine, P. (2018). Deep learning to represent subgrid processes in climate models. *Proceedings of the National Academy of Sciences*, *115*(39), 9684–9689.

Räty, O., Räisänen, J., Bosshard, T., & Donnelly, C. (2018). Intercomparison of univariate and joint bias correction methods in changing climate from a hydrological perspective. *Climate*, *6*(2), 33.

Rizzo, M. L., & Székely, G. J. (2016). Energy distance. *wiley interdisciplinary reviews: Computational statistics*, *8*(1), 27–38.

Ronneberger, O., Fischer, P., & Brox, T. (2015). U-net: Convolutional networks for biomedical image segmentation. In *International conference on medical image computing and computer-assisted intervention* (pp. 234–241).

Sadeghi, M., Nguyen, P., Hsu, K., & Sorooshian, S. (2020). Improving near real-time precipitation estimation using a u-net convolutional neural network and geographical information. *Environmental Modelling & Software*, *134*, 104856.

Salimans, T., Goodfellow, I., Zaremba, W., Cheung, V., Radford, A., & Chen, X. (2016). Improved techniques for training gans. *Advances in neural information processing systems*, *29*, 2234–2242.

Schneider, T., Lan, S., Stuart, A., & Teixeira, J. (2017). Earth system modeling 2.0: A blueprint for models that learn from observations and targeted high-resolution simulations. *Geophysical Research Letters*, *44*(24), 12–396.

Schneider, T., Stuart, A. M., & Wu, J.-L. (2020). Learning stochastic closures using ensemble kalman inversion. *arXiv preprint arXiv:2004.08376*.

Simonyan, K., Vedaldi, A., & Zisserman, A. (2013). Deep inside convolutional networks: Visualising image classification models and saliency maps. *arXiv preprint arXiv:1312.6034*.

Sippel, S., Meinshausen, N., Fischer, E. M., Székely, E., & Knutti, R. (2020). Climate change now detectable from any single day of weather at global scale. *Nature climate change*, *10*(1), 35–41.

Smith, L. A. (2001). Disentangling uncertainty and error: On the predictability of nonlinear systems. In *Nonlinear dynamics and statistics* (pp. 31–64). Springer.

Sun, A., & Tang, G. (2020). Downscaling satellite and reanalysis precipitation products using attention-based deep convolutional neural nets. *Front. Water 2: 536743. doi: 10.3389/frwa.*

Tapiador, F. J., Roca, R., Del Genio, A., Dewitte, B., Petersen, W., & Zhang, F. (2019). Is precipitation a good metric for model performance? *Bulletin of the American Meteorological Society*, *100*(2), 223–233.

Teutschbein, C., & Seibert, J. (2012). Bias correction of regional climate model simulations for hydrological climate-change impact studies: Review and evaluation of different methods. *Journal of hydrology*, *456*, 12–29.

Toms, B. A., Barnes, E. A., & Ebert-Uphoff, I. (2020). Physically interpretable neural networks for the geosciences: Applications to earth system variability. *Journal of Advances in Modeling Earth Systems*, *12*(9), e2019MS002002.

Tzeng, E., Hoffman, J., Saenko, K., & Darrell, T. (2017). Adversarial discriminative domain adaptation. In *Proceedings of the ieee conference on computer vision and pattern recognition* (pp. 7167–7176).

Van Horn, G., & Perona, P. (2017). The devil is in the tails: Fine-grained classification in the wild. *arXiv preprint arXiv:1709.01450*.

Wang, T.-C., Liu, M.-Y., Zhu, J.-Y., Liu, G., Tao, A., Kautz, J., & Catanzaro, B. (2018). Video-to-video synthesis. In *Proceedings of the 32nd international conference on neural information processing systems* (pp. 1152–1164).

Wetterhall, F., Pappenberger, F., He, Y., Freer, J., & Cloke, H. (2012). Conditioning model output statistics of regional climate model precipitation on circulation patterns. *Nonlinear Processes in Geophysics*, *19*(6), 623–633.

Weyn, J. A., Durran, D. R., & Caruana, R. (2019). Can machines learn to predict weather? using deep learning to predict gridded 500-hpa geopotential height from historical weather data. *Journal of Advances in Modeling Earth Systems*, *11*(8), 2680–2693.

Wilson, G., & Cook, D. J. (2020). A survey of unsupervised deep domain adaptation. *ACM Transactions on Intelligent Systems and Technology (TIST)*, *11*(5), 1–46.

Wolfram Research, Inc. (n.d.). *Mathematica 12.1.* Retrieved from `https://www.wolfram.com`

Wood, A. W., Leung, L. R., Sridhar, V., & Lettenmaier, D. (2004). Hydrologic implications of dynamical and statistical approaches to downscaling climate model outputs. *Climatic change*, *62*(1-3), 189–216.

Wu, J.-L., Kashinath, K., Albert, A., Chirila, D., Xiao, H., et al. (2020). Enforcing statistical constraints in generative adversarial networks for modeling chaotic dynamical systems. *Journal of Computational Physics*, *406*, 109209.

Xie, P., Chen, M., & Shi, W. (2010). Cpc unified gauge-based analysis of global daily precipitation. In *Preprints, 24th conf. on hydrology, atlanta, ga, amer. meteor. soc* (Vol. 2).

Xie, S., Ma, H.-Y., Boyle, J. S., Klein, S. A., & Zhang, Y. (2012). On the correspondence between short-and long-time-scale systematic errors in cam4/cam5 for the year of tropical convection. *Journal of Climate*, *25*(22), 7937–7955.

Yang, Z., Wu, J.-L., & Xiao, H. (2019). Enforcing deterministic constraints on generative adversarial networks for emulating physical systems. *arXiv preprint arXiv:1911.06671*.

Yuval, J., & O'Gorman, P. A. (2020). Stable machine-learning parameterization of subgrid processes for climate modeling at a range of resolutions. *Nature communications*, *11*(1), 1–10.

Zeiler, M. D., & Fergus, R. (2014). Visualizing and understanding convolutional networks. In *European conference on computer vision* (pp. 818–833).

Zelinka, M. D., Myers, T. A., McCoy, D. T., Po-Chedley, S., Caldwell, P. M., Ceppi, P., ... Taylor, K. E. (2020). Causes of higher climate sensitivity in cmip6 models. *Geophysical Research Letters*, *47*(1), e2019GL085782.

Zhang, J., Zheng, Q., Wu, L., & Zeng, L. (2020). Using deep learning to improve ensemble smoother: Applications to subsurface characterization. *Water Resources Research*.

Zhao, T., Chen, H., Pan, B., Ye, L., Cai, H., Zhang, Y., & Chen, X. (2021). Correspondence relationship between enso teleconnection and anomaly correlation for gcm seasonal precipitation forecasts. *Climate Dynamics*, 1–17.

Zhu, J.-Y., Park, T., Isola, P., & Efros, A. A. (2017). Unpaired image-to-image translation using cycle-consistent adversarial networks. In *Proceedings of the ieee international conference on computer vision* (pp. 2223–2232).

Acknowledgements

This work was performed under the auspices of the U.S. Department of Energy by Lawrence Livermore National Laboratory under contract DE-AC52-07NA27344. Lawrence Livermore National Security, LLC. The views expressed here do not necessarily reflect the opinion of the United States Government, the United States Department of Energy, or Lawrence Livermore National Laboratory. This work was supported by LLNL Laboratory Directed Research and Development project 19-ER-032. This document is released with IM tracking number LLNL-JRNL-817982. The Community Earth System Model version 2 (CESM2) historical simulation data are available through https://esgf-node.llnl.gov/projects/cmip6/. The CPC unified gauge-based analysis of daily precipitation data are available through https://psl.noaa.gov/data/gridded/data.cpc.globalprecip.html. The ECMWF atmospheric reanalysis of the 20th century (ERA-20C) data are available through https://www.ecmwf.int/en/forecasts/datasets/reanalysis-datasets/era-20c. We appreciate the valuable and comprehensive comments from two anonymous reviewers. The code is available through https://github.com/panbaoxiang/RADA.

Fig. 1 Adversarial learning of GCM biases. We consider the correction of daily precipitation projection over the contiguous United States as an example (see Sec. 3 for data sources and details). We randomly sample daily precipitation field maps (i.e., 03 January 1982) from the GCM historical simulation domain $\mathbf{X}$, and sample daily precipitation field maps in the same months and ± 5 years from the observation domain $\mathbf{Y}$ (i.e., 13 January 1983, we specify the time window of sampling to exclude the impact of seasonality and climate change.). The discriminator D learns to distinguish whether a sample comes from $\mathbf{Y}$ or $G(\mathbf{X})$ by minimizing the discrimination error using gradient descent (blue arrow). The bias corrector G learns to make the correction result $G(\mathbf{X})$ less distinguishable from $\mathbf{Y}$ through maximizing the discrimination error of D using gradient ascent (red arrow).

Fig. 2 Structure of the Regularized Adversarial Domain Adaptation (RADA) model. (a), overall structure of the model. The model applies a conditional generative adversarial network $\{G, D\}$ (red arrows) to obtain $G(\mathbf{X}, \mathbf{S}_\mathbf{X})$ that is identically distributed with $\mathbf{Y}$ as viewed by D. The adversarial learning is regularized by (i) coupling with an inverse model $\{G^{-1}, D^{-1}\}$ (blue arrows), and (ii) maintaining the coherency between resolved dynamics and the target variable (brown arrows). (b), U-net (Ronneberger et al., 2015) architecture of the submodules $F_\mathbf{X}$ and $F_\mathbf{Y}$. (c, d), Res-net (He et al., 2016) architecture of the submodules G, G^{-1} and D, D^{-1}.

Fig. 3 Bias correction results for the first to fourth order moments (a-d). Each sub-figure in (a-d) shows the spatial distributions of a considered index from observation (left), CESM2 simulation (middle), and RADA corrected CESM2 simulation (right). Stippling in CESM2 simulation shows locations where the original simulation better matches observation compared to bias corrections based on a bootstrap test, stippling in $\text{CESM2}_{\text{RADA}}$ shows locations where the bias correction better matches observation compared to original simulation. The spatial correlation coefficient and spatial average root mean square error (RMSE) between simulation-revealed precipitation indices and observation-revealed precipitation indices are calculated and denoted.

Fig. 4 Similar to Fig. 3 but for correcting the 33%, 66%, 99% quantile (a-c), and the probability of precipitation (d).

Fig. 5 Similar to Fig. 3 but for correcting the average intensity (a), 1-day, 3-day, and 5-day maximum precipitation (b-d).

Fig. 6 Similar to Fig. 3 but for the winter (a, December to January) and summer (b, June to August) precipitation ratio.

Fig. 7 Spatial loading of the first (a) and second (b) principal components (PCs) of the precipitation field. The variance explained by PC_1 and PC_2 are labeled on top of each map. The spatial correlation coefficient and spatial average root mean square error (RMSE) between simulation-revealed EOFs and observation-revealed EOFs are calculated and denoted.

Fig. 8 Applicability (correlation skill) of the statistical downscaling model $F^*_\mathbf{X}$ and $F^*_\mathbf{Y}$ for the observed and simulated precipitation field, where $F^*_\mathbf{X}$ and $F^*_\mathbf{Y}$ are U-net based statistical downscaling models trained using the CESM2 historical simulation data and observational data. The spatial correlation coefficient and spatial average root mean square error (RMSE) of the downscaling correlation skills are calculated and denoted.

Fig. 9 Relative spatial correlation skills for the 7 GAN-based bias correction models (a-g). The GAN-based baseline models are obtained by removing one or several regularizers on the RADA network architecture. The remaining regularizers for these models are denoted in the legend. For each model and each considered precipitation distribution characteristics, we calculate the spatial correlation between the observation-revealed precipitation indices and simulation-revealed precipitation indices. We re-scale the models' correlation skills to the range of [0, 1] using min-max normalization based on correlation skills achieved by the 7 baseline models, the original CESM2 simulation, and the RADA model. The skills of CESM2 orig-

inal simulation (gray dashed) and RADA corrected simulation (black) are plotted as benchmarks.

Fig. 10 Relative spatial correlation skills for (a) the *quantile mapping* approach, (b) the MBCn approach without early stopping, and (c) the MBCn approach with early stopping. For each model and each considered precipitation distribution characteristics, we calculate the spatial correlation between the observation-revealed precipitation indices and simulation-revealed precipitation indices. We re-scale the models' correlation skills to the range of [0, 1] using min-max normalization based on correlation skills achieved by the 3 baseline models, the original CESM2 simulation, and the RADA model. The skills of CESM2 original simulation (gray dashed) and RADA corrected simulation (black) are plotted as benchmarks.

Fig. 11 Top: randomly selected samples of precipitation observation maps (first row) and the CESM2 precipitation simulation maps before (second row) and after (third row) bias correction. Bottom: the performance of the human being test taker (top) and the deep neural network (bottom) for distinguishing observation samples and simulation samples before (left) and after (right) bias correction. TP, FP, TN, and FN are true positive rate, false positive rate, true negative rate, and false negative rate, respectively. The human being test is based on 200 samples, while the deep neural network test is based on 600 samples.

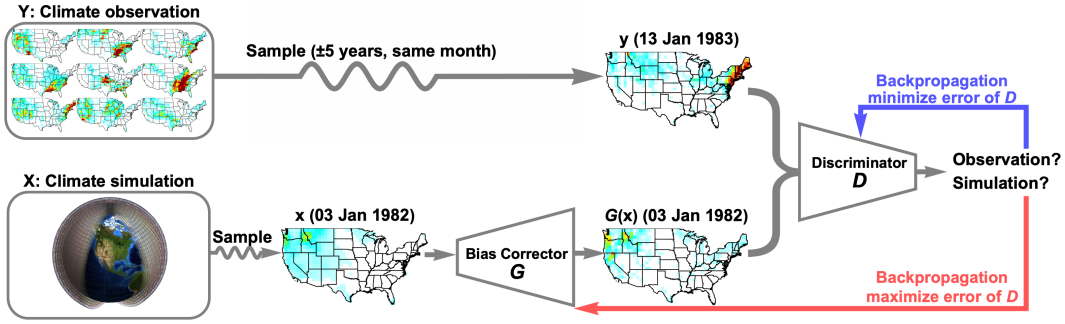

Figure 1. Adversarial learning of GCM biases. We consider the correction of daily precipitation projection over the contiguous United States as an example (see Sec. 3 for data sources and details). We randomly sample daily precipitation field maps (i.e., 03 January 1982) from the GCM historical simulation domain $\mathbf{X}$, and sample daily precipitation field maps in the same months and ± 5 years from the observation domain $\mathbf{Y}$ (i.e., 13 January 1983, we specify the time window of sampling to exclude the impact of seasonality and climate change.). The discriminator D learns to distinguish whether a sample comes from $\mathbf{Y}$ or $G(\mathbf{X})$ by minimizing the discrimination error using gradient descent (blue arrow). The bias corrector G learns to make the correction result $G(\mathbf{X})$ less distinguishable from $\mathbf{Y}$ through maximizing the discrimination error of D using gradient ascent (red arrow).

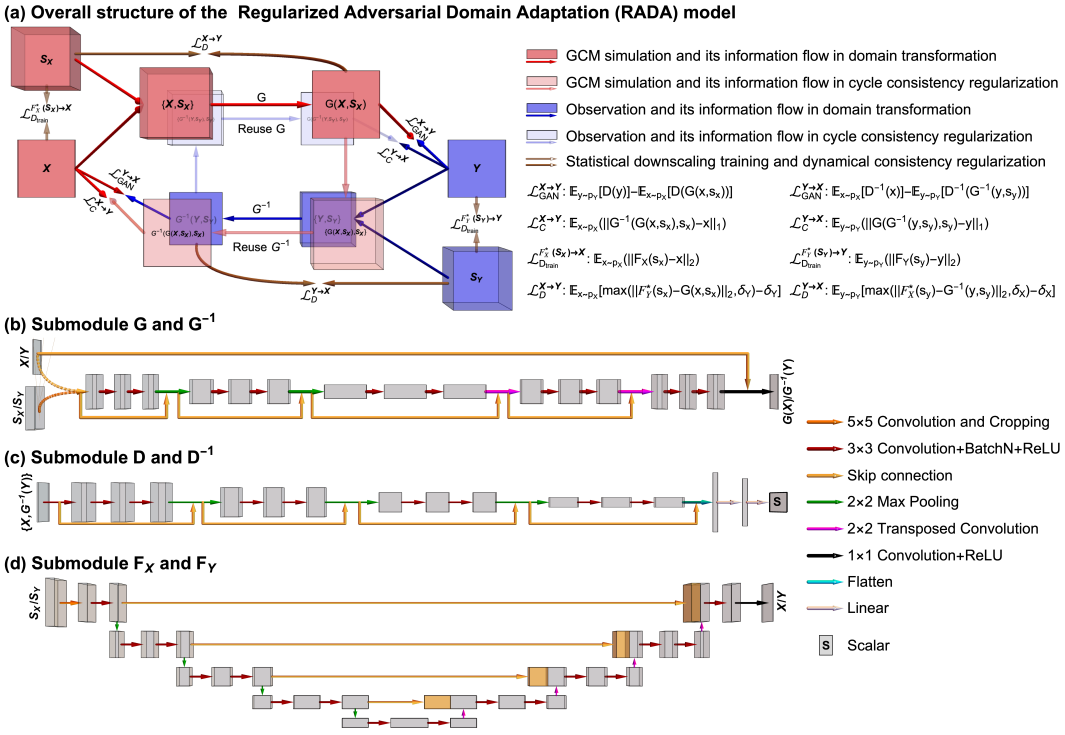

Figure 2. Structure of the Regularized Adversarial Domain Adaptation (RADA) model. (a), overall structure of the model. The model applies a conditional generative adversarial network $\{G, D\}$ (red arrows) to obtain $G(\mathbf{X}, \mathbf{S_X})$ that is identically distributed with $\mathbf{Y}$ as viewed by D. The adversarial learning is regularized by (i) coupling with an inverse model $\{G^{-1}, D^{-1}\}$ (blue arrows), and (ii) maintaining the coherency between resolved dynamics and the target variable (brown arrows). (b), U-net (Ronneberger et al., 2015) architecture of the submodules $F_{\mathbf{X}}$ and $F_{\mathbf{Y}}$. (c, d), Res-net (He et al., 2016) architecture of the submodules G, G^{-1} and D, D^{-1}.

.

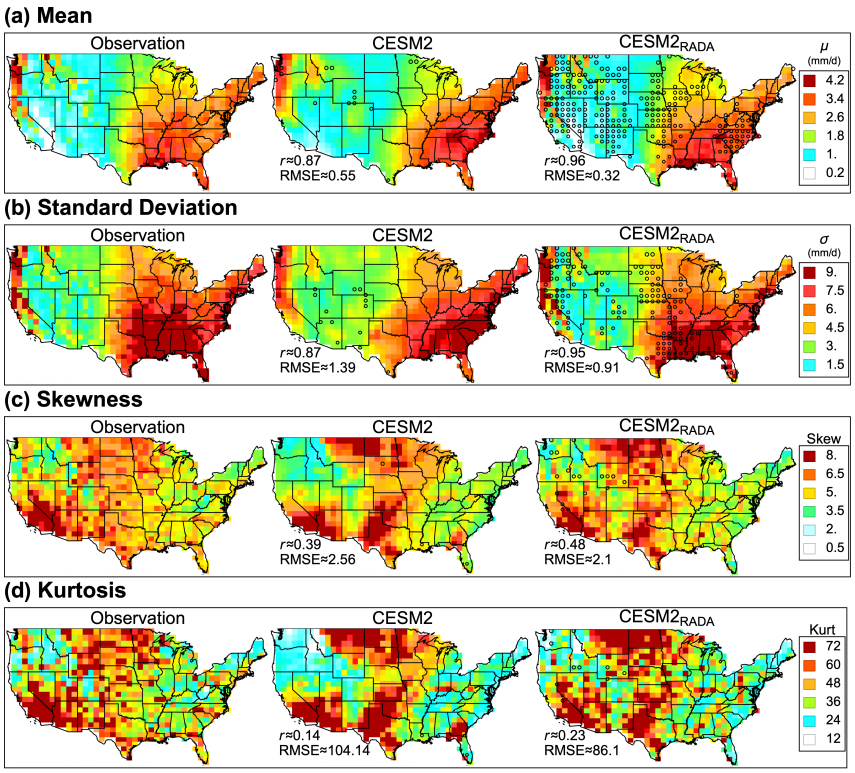

Figure 3. Bias correction results for the first to fourth order moments (a-d). Each sub-figure in (a-d) shows the spatial distributions of a considered index from observation (left), CESM2 simulation (middle), and RADA corrected CESM2 simulation (right). Stippling in CESM2 simulation shows locations where the original simulation better matches observation compared to bias corrections based on a bootstrap test, stippling in $\mathrm{CESM2_{RADA}}$ shows locations where the bias correction better matches observation compared to original simulation. The spatial correlation coefficient and spatial average root mean square error (RMSE) between simulation-revealed precipitation indices and observation-revealed precipitation indices are calculated and denoted.

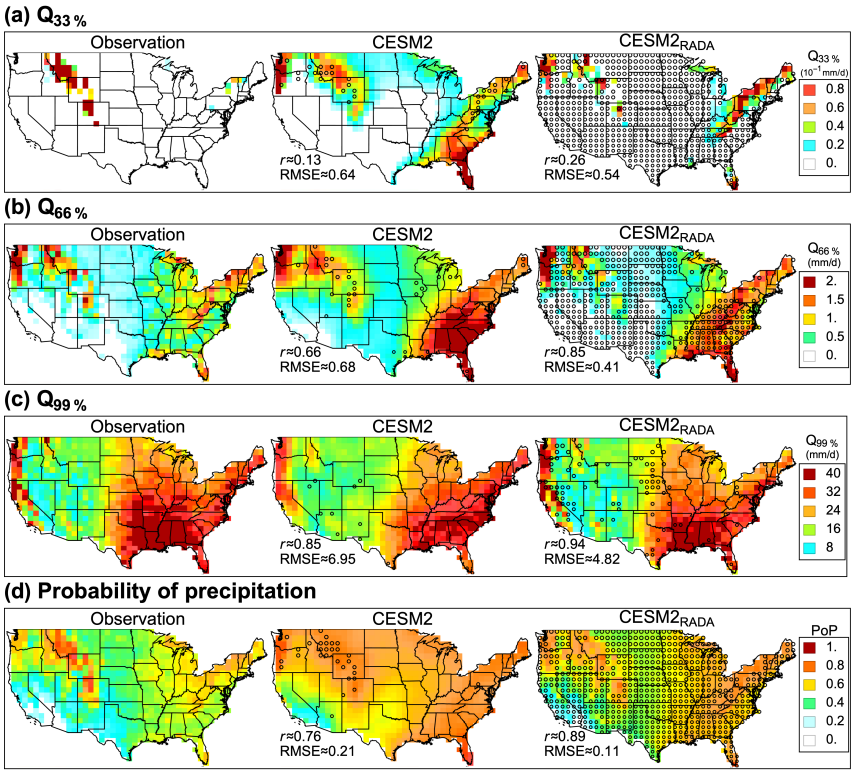

Figure 4. Similar to Fig. 3 but for correcting the 33%, 66%, 99% quantile (a-c), and the probability of precipitation (d).

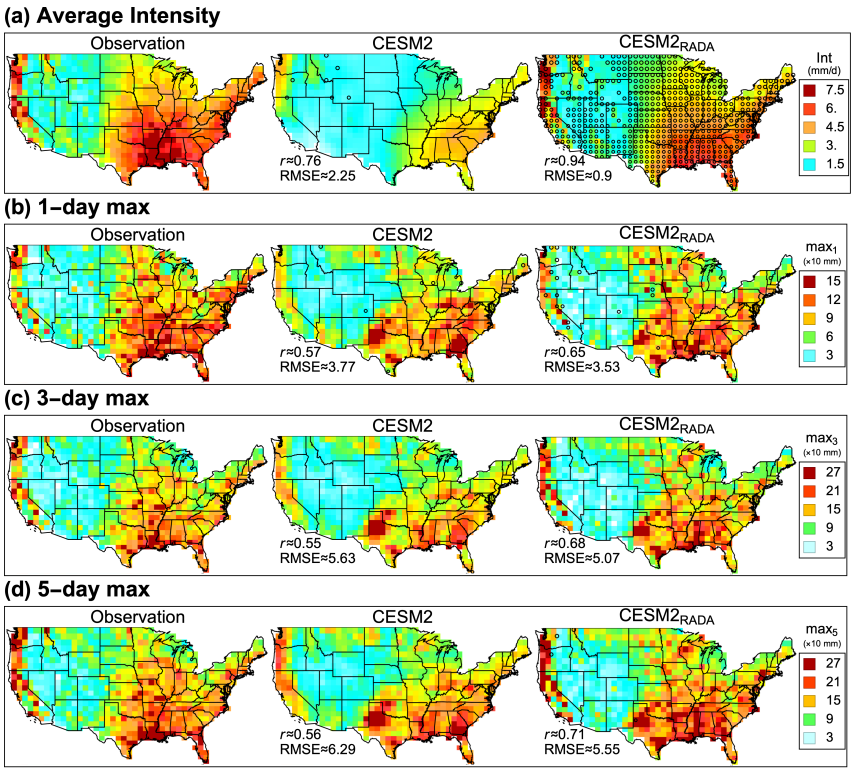

Figure 5. Similar to Fig. 3 but for correcting the average intensity (a), 1-day, 3-day, and 5-day maximum precipitation (b-d).

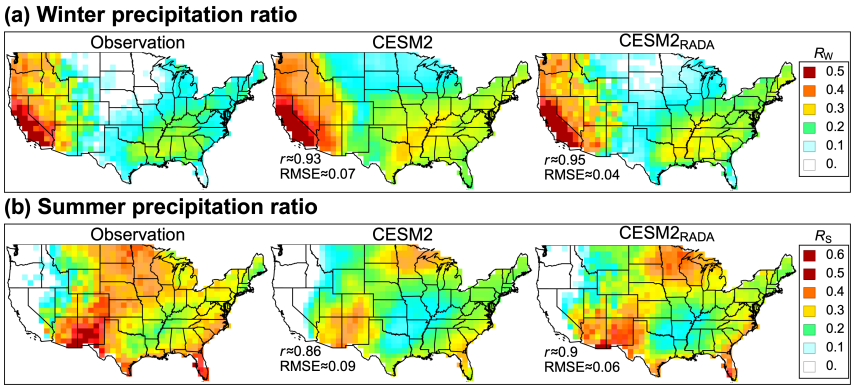

Figure 6. Similar to Fig. 3 but for the winter (a, December to January) and summer (b, June to August) precipitation ratio.

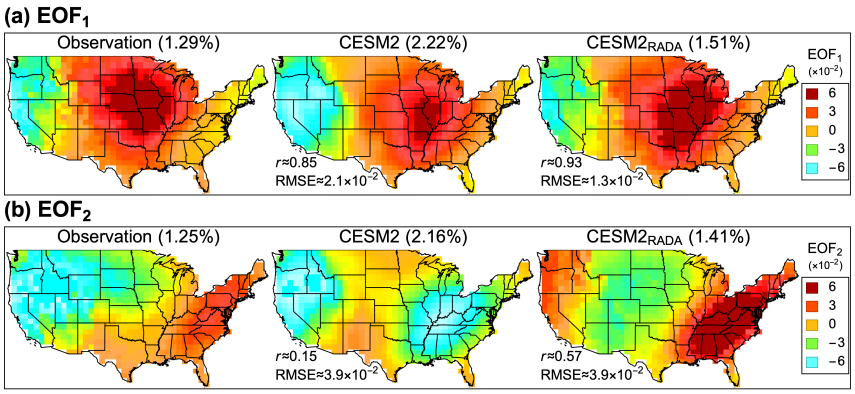

Figure 7. Spatial loading of the first (a) and second (b) principal components (PCs) of the precipitation field. The variance explained by PC_1 and PC_2 are labeled on top of each map. The spatial correlation coefficient and spatial average root mean square error (RMSE) between simulation-revealed EOFs and observation-revealed EOFs are calculated and denoted.

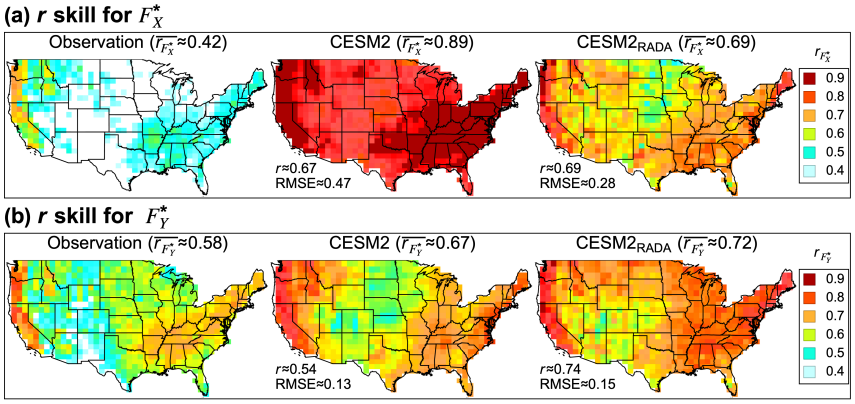

Figure 8. Applicability (correlation skill) of the statistical downscaling model $F^*_{\mathbf{X}}$ and $F^*_{\mathbf{Y}}$ for the observed and simulated precipitation field, where $F^*_{\mathbf{X}}$ and $F^*_{\mathbf{Y}}$ are U-net based statistical downscaling models trained using the CESM2 historical simulation data and observational data. The spatial correlation coefficient and spatial average root mean square error (RMSE) of the downscaling correlation skills are calculated and denoted.

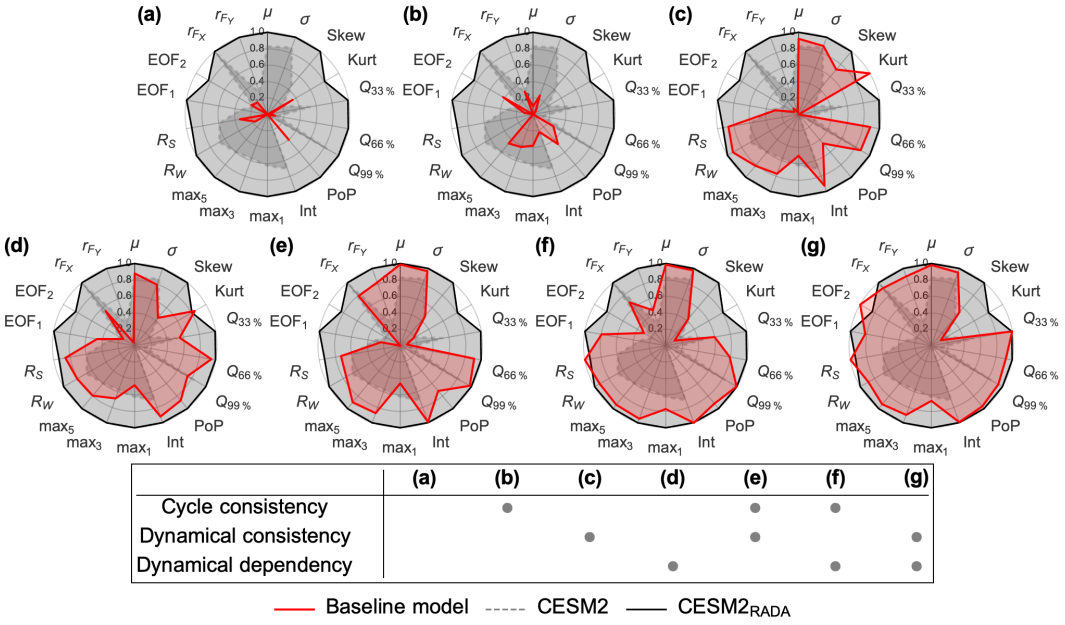

Figure 9. Relative spatial correlation skills for the 7 GAN-based bias correction models (a-g). The GAN-based baseline models are obtained by removing one or several regularizers on the RADA network architecture. The remaining regularizers for these models are denoted in the legend. For each model and each considered precipitation distribution characteristics, we calculate the spatial correlation between the observation-revealed precipitation indices and simulation-revealed precipitation indices. We re-scale the models' correlation skills to the range of [0, 1] using min-max normalization based on correlation skills achieved by the 7 baseline models, the original CESM2 simulation, and the RADA model. The skills of CESM2 original simulation (gray dashed) and RADA corrected simulation (black) are plotted as benchmarks.

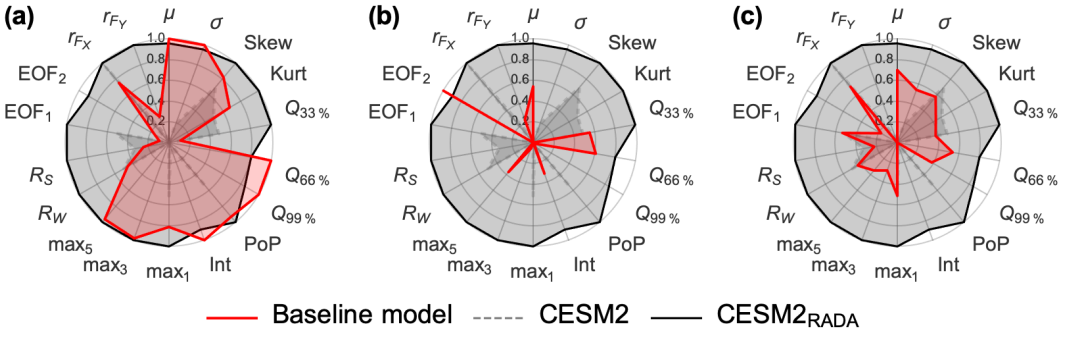

Figure 10. Relative spatial correlation skills for (a) the *quantile mapping* approach, (b) the MBCn approach without early stopping, and (c) the MBCn approach with early stopping. For each model and each considered precipitation distribution characteristics, we calculate the spatial correlation between the observation-revealed precipitation indices and simulation-revealed precipitation indices. We re-scale the models' correlation skills to the range of [0, 1] using min-max normalization based on correlation skills achieved by the 3 baseline models, the original CESM2 simulation, and the RADA model. The skills of CESM2 original simulation (gray dashed) and RADA corrected simulation (black) are plotted as benchmarks.

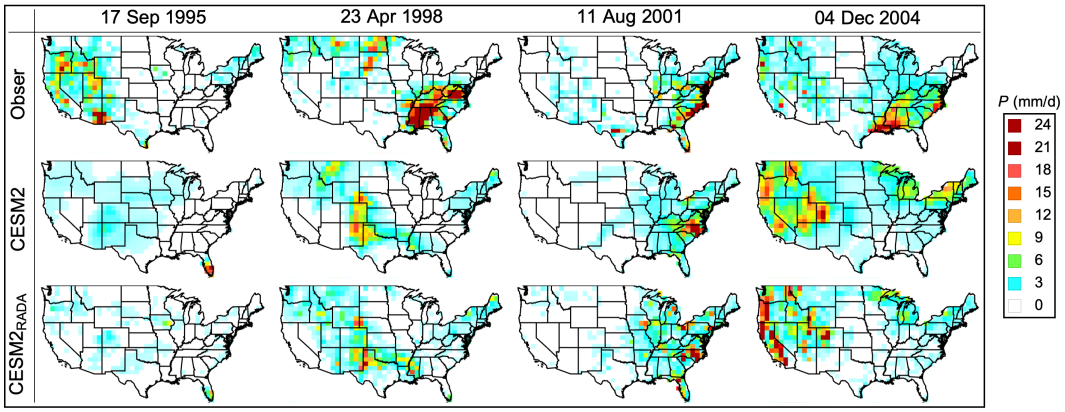

		Before bias correction		After bias correction	
Human being (200 samples)		**Actual class**		**Actual class**	
	Predicted	Obser	CESM2	Obser	$CESM2_{RADA}$
	Obser	TP=93.45%	FP=4.30%	TP=78.72%	FP=67.92%
	CESM2 / $CESM2_{RADA}$	FN=3.55%	TN=95.70%	FN=21.28%	TN=32.08%
Deep neural network (600 samples)		**Actual class**		**Actual class**	
	Predicted	Obser	CESM2	Obser	$CESM2_{RADA}$
	Obser	TP=99.97%	FP=0.00%	TP=78.75%	FP=9.43%
	CESM2 / $CESM2_{RADA}$	FN=0.03%	TN=100.%	FN=21.25%	TN=90.57%

Figure 11. Top: randomly selected samples of precipitation observation maps (first row) and the CESM2 precipitation simulation maps before (second row) and after (third row) bias correction. Bottom: the performance of the human being test taker (top) and the deep neural network (bottom) for distinguishing observation samples and simulation samples before (left) and after (right) bias correction. TP, FP, TN, and FN are true positive rate, false positive rate, true negative rate, and false negative rate, respectively. The human being test is based on 200 samples, while the deep neural network test is based on 600 samples.